GEOLOGICAL JOURNAL
Geol. J. **44**: 167–190 (2009)
Published online 16 January 2009 in Wiley InterScience
(www.interscience.wiley.com) DOI: 10.1002/gj.1145

Deformation history of the eclogite- and jadeitite-bearing mélange from North Motagua Fault Zone, Guatemala: insights in the processes of a fossil subduction channel

MICHELE MARRONI [1,2]*, ***LUCA PANDOLFI*** [1,2], ***GIANFRANCO PRINCIPI*** [2,3], ***ALESSANDRO MALASOMA*** [1] ***and FRANCESCA MENEGHINI*** [1]

[1] *Dipartimento di Scienze della Terra, Università di Pisa, Italy*
[2] *Istituto di Geoscienze e Georisorse, CNR, Italy*
[3] *Dipartimento di Scienze della Terra, Università di Firenze, Italy*

In Guatemala, along the northern side of the Motagua Valley, a mélange consisting of blocks of eclogite and jadeitite set in a metaserpentinitic and metasedimentary matrix crops out. The metasedimentary rocks display a complex deformation history that includes four tectonic phases, from D1 to D4. The D1 phase occurs only as a relic and is characterized by a mineral assemblage developed under pressure temperature (P–T) conditions of 1.00–1.25 GPa and 206–263°C. The D2 phase, characterized by isoclinal folds, schistosity and mineral/stretching lineation, developed at P–T conditions of 0.70–1.20 GPa and 279–409°C. The following D3 and D4 phases show deformations developed at shallower structural levels. Whereas the D1 phase can be interpreted as the result of underplating of slices of oceanic lithosphere during an intraoceanic subduction, the following phases have been acquired by the mélange during its progressive exhumation through different mechanisms. The deformations related to the D2 and D3 phases can be regarded as acquired by extrusion of the mélange within a subduction channel during a stage of oblique subduction. In addition, the structural evidences indicate that the coupling and mixing of different blocks occurred during the D2 phase, as a result of flow reverse and upward trajectory in the subduction channel. By contrast, the D4 phase can be interpreted as related to extension at shallow structural levels. In this framework, the exhumation-related structures in the mélange indicate that this process, probably long-lived, developed through different mechanisms, active in the subduction channel through time. Copyright © 2009 John Wiley & Sons, Ltd.

Received 18 January 2008; accepted 29 October 2008

KEY WORDS high-pressure metamorphism; mélange; subduction; exhumation; subduction channel; Motagua Fault Zone; Guatemala

1. INTRODUCTION

Accretionary prisms represent the most dynamic element in convergent margins, and are continuously shaped by two main tectono-metamorphic processes: (i) the accretion, i.e. the transfer of material from the downgoing to the upper plate that promotes the horizontal (frontal accretion) and vertical (underplating) growing of the prism, and (ii) the tectonic erosion, through which material previously accreted is removed from the prism base and underthrust at depth (Von Huene and Scholl 1991; Cloos and Shreve 1988; Clift and Vannucchi 2004).

The exhumation processes, providing the transfer of material from the prism interior to the surface, complete this complex mass circulation in and across the prism and represent a crucial but not well-monitored step in the prism evolution. Different models for the exhumation of the previously accreted materials has been proposed, including essentially ductile extrusion of tectonic units at the prism base (e.g. Chemenda *et al*. 1995; Thompson *et al*. 1997a;

* Correspondence to: M. Marroni, Dipartimento di Scienze della Terra, Università di Pisa, Via S. Maria, 53–56126 Pisa, Italy.
E-mail: marroni@dst.unipi.it

Ernst 1999), extrusion of high-grade blocks embedded in a matrix (e.g. Cloos 1982; Cloos and Shreve 1988; Schwartz *et al*. 2001; Gerya *et al*. 2002; Gorczyk *et al*. 2007), tectonic extension of the shallower portion of the prism (Platt 1986, 1993) and material upward flow at the prism rear driven by the backstop geometry of the upper plate (Pavlis and Bruhn 1983; Allemand and Lardeaux 1997).

Although many geological and geophysical studies on present-day subduction zones have highlighted lots of aspects of the shallower portions of many active prisms, the tectonic processes at deeper levels, as well as those connected with exhumation, cannot be monitored on active margins. On the contrary, ancient accretionary complexes preserve integrated structural histories spanning the evolution of subducting sediments through burial, compaction, dewatering, shearing, accretion and intra-wedge deformation and exhumation. Extensive mélange units commonly characterize these preserved complexes. Forming during shear localization at the plate boundary, these mélanges have been interpreted as palaeo-décollements (Silver *et al*. 1985; Fisher and Byrne 1987; Moore and Byrne 1987; Kimura *et al.* 1992) and their formation well explained in the subduction channel model (Cloos and Shreve 1988). The central assumption of the subduction channel model is that material deforms as a viscous fluid and is then dragged by the descending plate beneath the overriding crystalline plate. This downgoing material can, under certain conditions, be turned back in a thick zone of reverse flow along the rigid roof of the channel. The high shear strain during reversal of direction may not only cause mélange formation but also entrain large sheets of previously accreted, then already metamorphosed, material (e.g. Schwartz *et al*. 2001; Gorczyk *et al*. 2007).

In this paper, a reconstruction of the tectono-metamorphic history of a metamorphosed eclogite- and jadeitite-bearing mélange, from the North Motagua Fault Zone of Guatemala, is proposed, in order to provide useful insights for the reconstruction of the exhumation processes developed into the accretionary prism. A possible subduction channel setting is envisioned as responsible for high-grade units exhumation through incorporation into the subduction mélange.

2. GEODYNAMIC SETTING OF THE GUATEMALA OPHIOLITES

The high-pressure metaophiolites preserved as deformed and metamorphosed slices in collisional belts are regarded as fundamental markers for geodynamic reconstructions. The Caribbean area displays well-developed metaophiolitic sequences, mainly at the southern and northern margins of the Caribbean Plate, where collisional belts of Alpine age crop out (Figure 1). These ophiolite sequences are interpreted as remnants of the proto-Caribbean oceanic basin developed after the breakup of Pangea during the Jurassic-Early Cretaceous and subsequently involved in the Eo-Caribbean tectonic events of 'mid' Cretaceous–Early Tertiary age (e.g. Dengo 1985; Burke 1988; Pindell *et al*. 1988; Pindell and Barrett 1990; Meschede and Frisch 1998; Giunta *et al*. 2003). Both the southern and northern Caribbean margins record a long-lived tectonic history achieved in an oblique setting, where events of subduction, accretion and exhumation developed (e.g. Avé Lallemant and Guth 1990; Giunta *et al*. 2003 and references therein).

A segment of the northern margin of the Caribbean Plate crops out in Guatemala (Figure 1), where the boundary between the Maya microplate, belonging to the North American Plate, and the Chortis microplate, belonging to the Caribbean Plate, is represented by a complex, east–west trending, left-lateral strike fault zone (Dengo 1985; Donnelly *et al*. 1990; Beccaluva *et al*. 1995; Giunta *et al*. 2003; Harlow *et al*. 2004). This fault zone can be subdivided into three main strands: the Polochic Fault in the north, the Motagua–Cabanas Fault in the middle and the Jocotan–Chamelecon Fault in the south (Figures 2 and 3). The Motagua–Cabanas Fault Zone (MFZ), representing the main segment, is defined by widespread occurrence of ophiolitic units both at its northern and southern sides. These ophiolites represent the remnants of a fossil subduction zone developed in the Late Cretaceous–Early Tertiary time span at the northern border of the Carribbean Plate (Donnelly *et al*. 1990). The MFZ is thus regarded as a suture zone developed during the Cretaceous–Early Tertiary collisional events that led to the complete disruption of an oceanic domain located between the Maya and the Chortis microplates. Since Middle Tertiary, an east–west trending sinistral strike-slip tectonics resulted in a strong deformation and modification of the suture zone.

DOI: 10.1002/gj

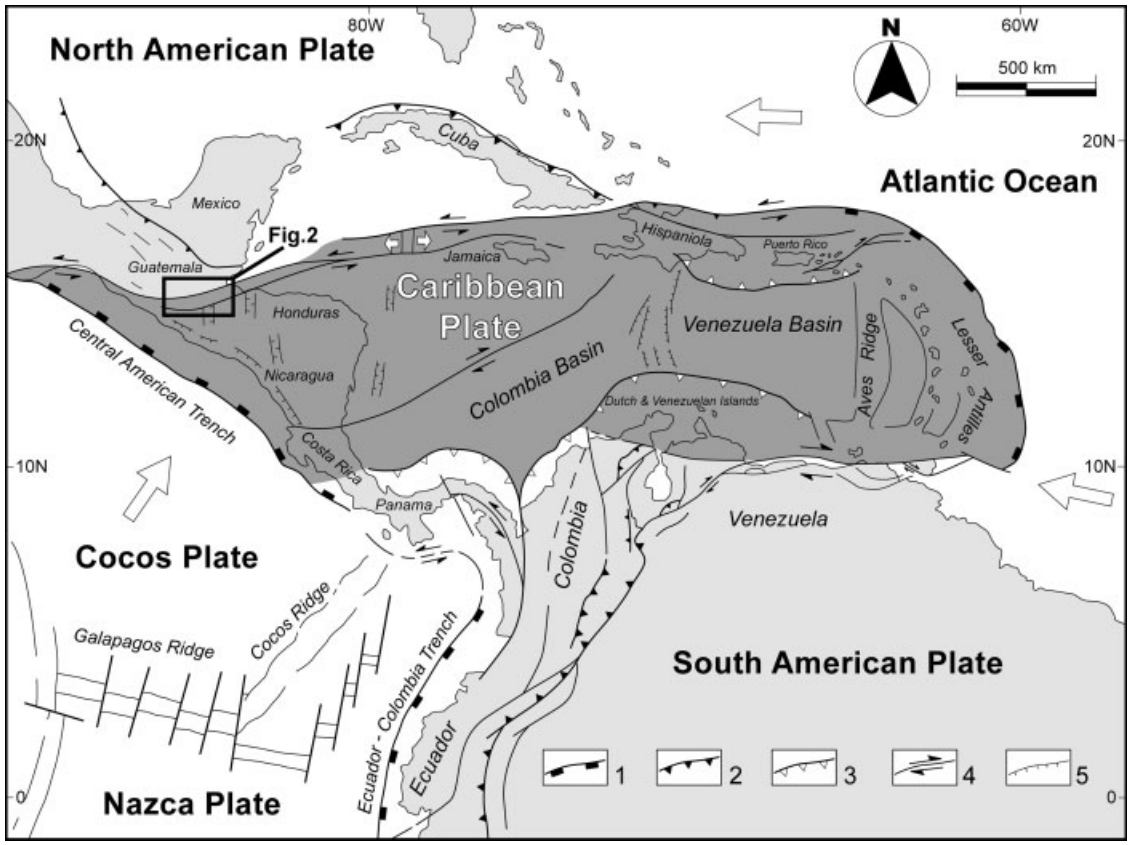

Figure 1. Tectonic sketch of the Caribbean Plate. Arrows indicate the prevalent directions of the plate movements. The main active tectonic features are also shown: (1) trenches and subduction zones; (2) frontal thrusts; (3) Tertiary accretionary prism; (4) strike-slip faults and (5) extensional faults (redrawn from Giunta *et al*. 2003).

Several ophiolitic bodies and regional-scale mega-boudins have been identified along the Motagua Fault Zone (Figure 2), associated with fragments of the Maya and Chortis continental crust (Beccaluva *et al*. 1995; Giunta *et al*. 2002; Harlow *et al*. 2004). The ophiolitic units, overthrusting the Maya microplate towards the north (Juan de la Paz, Baja Vera Paz and Sierra de Santa Cruz units) are characterized by island arc tholeiite (IAT) affinity that points to their origin in a supra-subduction setting. These ophiolites are affected by very low-grade metamorphism and weak deformations. By contrast, the ophiolitic slices found at the immediately northern and southern sides of the Motagua Fault Zone are characterized by strong deformations acquired under high-pressure (HP) metamorphic conditions. In addition, these metaophiolites show a mid-ocean ridge (MOR) geochemical signature that suggests an origin in an oceanic domain not connected with a subduction zone. In the model proposed by Beccaluva *et al*. (1995) the high-pressure/low-temperature (HP/LT) metaophiolites are regarded as the remnants of an accretionary prism related to an intraoceanic subduction zone of Early Cretaceous age. This subduction was probably north dipping, i.e. below the Maya microplate, according to the present-day location of IAT ophiolites. In the Tertiary, the continental collision and the subsequent sinistral strike-slip displacement between the Maya and Chortis microplates dismembered the pre-existing accretionary prism producing the present-day setting of the MFZ, where both sides are characterized by mélange with HP blocks dispersed in a serpentinite-rich matrix. This setting is similar to those observed in other belts located along the northern boundary of the Caribbean Plate, i.e. the Greater Antilles belt cropping out in the Cuba and Hispaniola islands (e.g. Schneider *et al*. 2004; Gorczyk *et al*. 2007; Krebs *et al*. 2008). This belt is characterized by the presence of an ophiolitic mélange affected by HP/LT metamorphism

DOI: 10.1002/gj

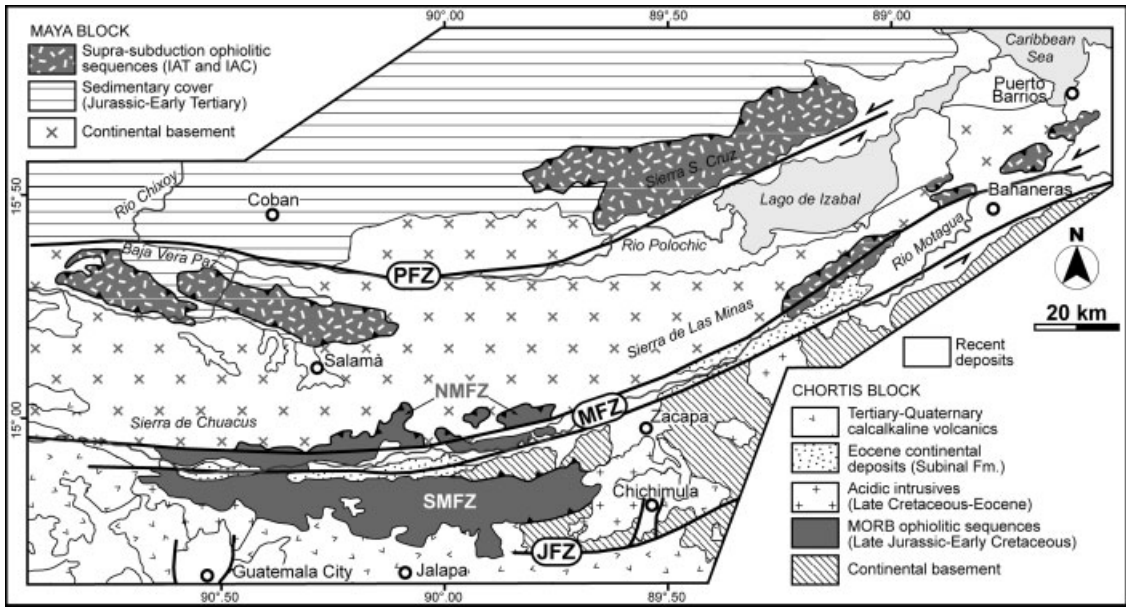

Figure 2. Tectonic sketch of the Rio Motagua area (eastern Guatemala). PFZ: Polochic Fault; MFZ: Motagua-Cabanas Fault; JFZ: Jocotan-Chamelecon Fault; SMFZ: South Motagua Fault Zone; NMFZ: North Motagua Fault Zone.

(Northern Serpentinite Mélange), interpretable as the eastward prolongation of the MFZ mélanges, before disruption by the strike-slip faults system.

Recent data (Harlow *et al*. 2004) have highlighted several differences between the blocks occurring in the northern and southern mélanges from the MFZ. Whereas in the southern side of the MFZ (hereafter the SMFZ) the blocks are represented by jadeitite, lawsonite-bearing eclogite and garnet-lawsonite blueschists set in a matrix of antigorite schists, in the northern side (hereafter the NMFZ) the blocks consist of jadeitite and amphibolitized eclogite enclosed in metaserpentinite and metasedimentary matrix. In addition, $^{40}Ar/^{39}Ar$ geochronological data on phengitic mica indicate that the metaophiolites are characterized by a different age of metamorphic re-equilibration. In the NMFZ the metaophiolites display an age of 77–65 Ma, whereas in SMFZ Harlow *et al*. (2004) detected an age of 125–113 Ma. The authors suggest that these different ages indicate the occurrence of two HP/LT

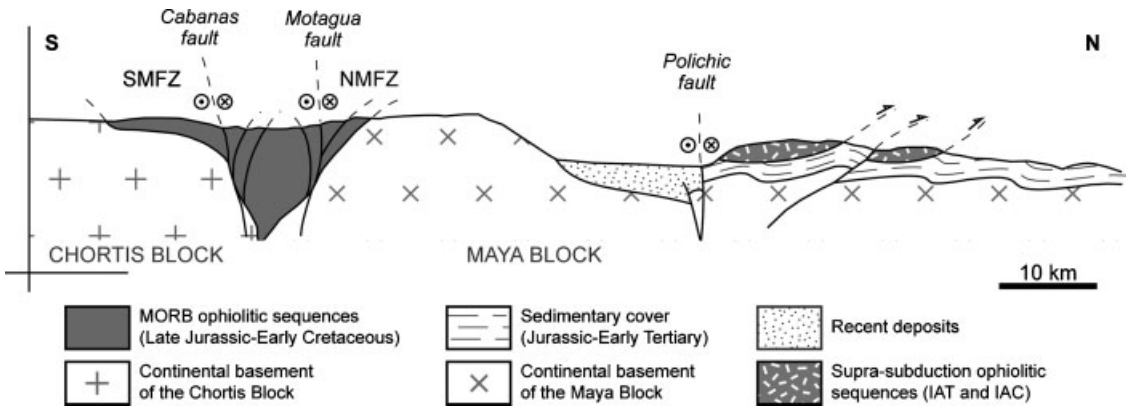

Figure 3. Interpretative cross-section showing the main tectonic units of the Rio Motagua area. SMFZ: South Motagua Fault Zone and NMFZ: North Motagua Fault Zone.

DOI: 10.1002/gj

metamorphic complexes originated during different subduction events and juxtaposed by the Tertiary strike-slip displacement along the MFZ.

3. THE MÉLANGE FROM NORTH MOTAGUA FAULT ZONE

In the northern side of the MFZ, the metaophiolites are generally represented by several metre-long blocks of eclogite and jadeitite set in a dominant metasedimentary matrix. This matrix mainly consists of quartzites and micaschists, even if levels of paragneisses and marbles have been recognized. A complete transition from pure quartzite to mica-rich quartzite, quartz-rich micaschist and micaschist has been detected. Locally, the matrix embedding the eclogitic and jadeititic blocks is represented by antigorite-bearing metaserpentinites. The protoliths of the metaserpentinites were lherzolites, whereas the eclogites derived from basic rocks with MOR affinity, were probably basalts and gabbros (Beccaluva *et al*. 1995). All these lithologies were derived from an oceanic lithosphere (metaserpentinites and eclogites) and related metasedimentary cover (quartzites, micaschists, paragneisses and marbles). Whereas the protolith of the pure quartzites and mica-rich quartzites are probably radiolarites of Late Jurassic age, as found in the SMFZ by Chiari *et al*. (2007), the quartz-rich micaschists, micaschists and paragneisses can be regarded as derived from pelagic turbidite sediments as shales, siltites and arenites. The protoliths of the marble layers, very rare in the field, are probably derived from carbonate turbidites interbedded with the pelagic sediments.

The eclogites are represented by paragonite-bearing zoisite eclogite. They are characterized by coarse-grained massive texture with a grain size of up to 1 cm. The climax metamorphic assemblage is represented by a garnet (Grt), omphacite (Omp), zoisite (Zo), phengite (Phe), paragonite (Pg), rutile (Rt) and quartz (Qtz) association. A metamorphic climax P–T conditions of 2.0–2.3 GPa and 600–650°C has been estimated for these rocks (Tsujimori *et al*. 2004). Amphibolite-facies metamorphic minerals, including neoblasts of garnet, overprinted these eclogites during decompression.

In turn, the jadeitites consist mostly of jadeite (Jd), with minor omphacite, phengite, paragonite and rutile. The jadeitites were originated at $100 < T < 400$°C and $0.5 < P < 1.1$ GPa (Harlow 1994). The origin of the jadeitites is still under debate. These rocks are generally regarded as the result of high-pressure metamorphism of plagiogranites, but Harlow *et al*. (2003 and references therein) have suggested an origin from crystallization of fluid in the subduction channel under high-pressure conditions. The jadeitites are affected by a decompressional history with growth of analcime, albite (Ab), amphibole (Amp), clinozoisite and nepheline. A further stage in the decompressional history is recorded by an assemblage consisting of albite, actinolite, zoisite, phengite, chlorite (Chl), K-feldspar and quartz developed at $T < 400$°C and $0.3 < P < 0.8$ GPa (Harlow 1994).

On the whole, the NMFZ rock assemblage can be described as a tectonic mélange where inclusion of blocks (eclogite and jadeitite) characterized by different P–T conditions of the metamorphic climax are set in a matrix consisting of metasedimentary rocks and metaserpentinites. Whereas the reconstruction of the deformation history in the metaserpentinites is hampered by the lithological features of these rocks and by their diffuse serpentinization, the metasedimentary rocks display well-preserved structural features crucial for the reconstruction of the deformation history of the mélange.

4. THE TECTONO-METAMORPHIC FEATURES OF NMFZ METASEDIMENTARY ROCKS

4.1. Mesoscale deformation history

The fabric elements of the D1 phase are poorly preserved due to the strong transposition related to the subsequent deformations, mainly those belonging to D2 phase. However, relics of the S1 continuous foliation are seldom preserved in the low-strain domains detected in some outcrops of quartz-rich micaschists and paragneisses. No meso-scale F1 folds have been recognized in the field.

DOI: 10.1002/gj

The most widespread structures detected in the field are those related to D2 phase that consists of F2 folds and associated S2 foliation and L2 lineation. As a result of the D2 phase, the lithological layers, mainly in the quartz-rich micaschists, micaschists and paragneisses, are strongly folded by the F2 folds, whose size range from a few centimetres up to 1 m. These folds deform also a set of pre-D2 quartz veins characterized by a granoblastic texture. The F2 folds, showing approximately similar geometry (class 2 and 3 of Ramsay 1967), are generally rootless with acute hinge zones and strongly thinned limbs (Figure 4a). They are mainly isoclinal in the quartz-rich micaschists, micaschists and paragneisses, whereas in the quartzites they range from isoclinal to subisoclinal. The limbs of the F2 folds are affected by boudinage, necking and pinch-and-swell structures (Figure 4b). In several outcrops, the boudins are rotated along the main foliation. The A2 axes are characterized by a ENE–WSW trend (A2 of Figure 5). However, the most widespread structural element of the D2 phase is represented by the S2 continuous foliation that can be recognized as the most prominent surface in all the studied outcrops. This foliation contains a L2 mineral/stretching lineation defined by prolate aggregates of quartz grains as well as preferred orientation of HP undeformed mineral grains such as lawsonite and white mica aggregates. This mineral/stretching lineation shows a well-defined ENE–WSW trend (L2 of Figure 5). This trend can be regarded as the primary one because it was not re-oriented during the following phases, according to coaxiality of the D2, D3 and D4 phases. Moreover, the parallelism between A2 axes and L2 mineral/stretching lineation suggests that the F2 folds are sheath-like folds. Parallel to the S2 foliation shear zones represented by mylonites and showing a top-to-the-south shear sense have been detected.

At the meso-scale the D2 phase-related structures are deformed by the D3 phase. This phase is characterized by the development of F3 subisoclinal to close to isoclinal folds characterized by rounded to subrounded hinges (Figure 4c). The D3 folds developed mainly in the quartz-rich micaschists, micaschists and in the paragneisses, whereas in the marble and in the quartzites they are rare. They are characterized by an approximately parallel geometry (class 1B and 1C of Ramsay 1967). Large-scale structures related to D3 phase have been identified in the map, mainly highlighted by the change in strike and dipping of the S2 foliation. The A3 axes strike about

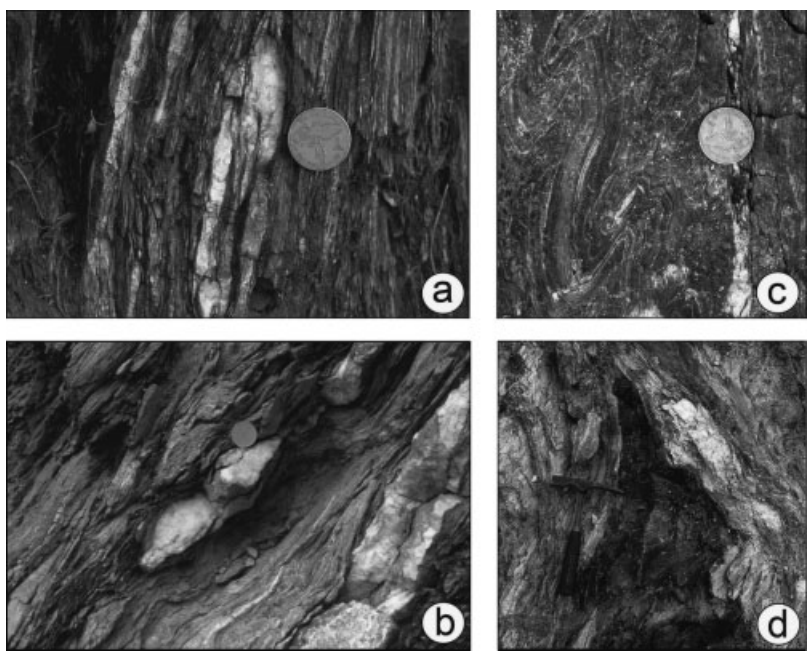

Figure 4. Meso-scale structures in the metasedimentary rocks from the North Motagua Fault Zone: (a) Hinge zone of a F2 isoclinal fold. Scale: coin is 21 mm; (b) Boudinage structures along the limb of a F2 fold. Scale: coin is 21 mm; (c) Asymmetric F3 folds. Scale: coin is 21 mm and (d) Interference pattern between isoclinal F2 and open F4 folds. Scale: hammer is 30 cm.

DOI: 10.1002/gj

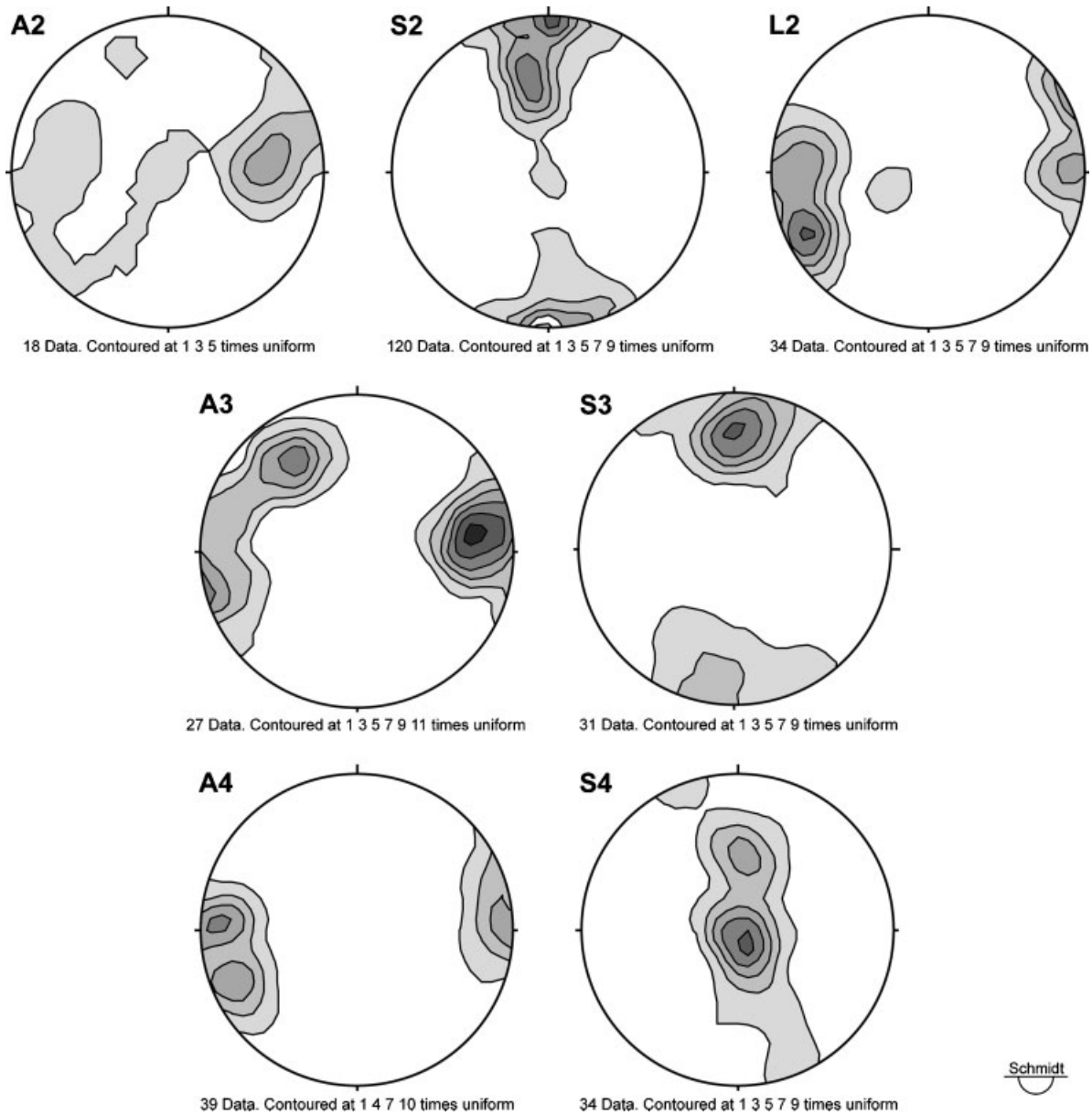

Figure 5. Stereographic representation of the main structural elements in the metasedimentary rocks from the North Motagua Fault Zone.

ENE–WSW with variable plunge angles (A3 of Figure 5), whereas AP3 axial planes are steeply inclined with predominately ENE–WSW strikes (S3 of Figure 5). The F3 folds are associated to a spaced S3 convergent fanning axial-plane foliation that can be classified as a crenulation cleavage in the micaschists and as disjunctive cleavage in the more competent lithologies, as the marbles.

The following D4 phase is represented by structures that slightly modified the former structural setting. These structures are mainly represented by open to tight parallel F4 folds (Figure 4d), although some minor scale kink-folds occur. The A4 fold axes are sub-horizontal clustering around a ENE–WSW trend (A4 of Figure 5), whereas the AP4 axial planes are predominately sub-horizontal (S4 of Figure 5). Associated to the F4 folds, low-angle shear

DOI: 10.1002/gj

zones characterized by brittle structures are widespread. These shear zones, when restored from subsequent deformation phase, display a normal fault motion with a top-to-the-NNW sense of shear.

According to Giunta *et al*. (2003), the pre-Eocene age of all these phases is pointed out by the occurrence of the Subinal Fm. (Eocene), an unmetamorphosed clastic deposit unconformably covering the tectonic units from the Motagua Fault Zone.

The following post-Eocene deformations, probably ranging in age from Miocene to Quaternary, are represented by strike-slip faults and the associated structures, not discussed in this paper.

4.2. Microstructures and metamorphic petrography

Investigated samples consist of metasedimentary rocks that can be classified as quartzite, mica-rich quartzite, quartz-rich micaschist and micaschist (Table 1). The quartzites and mica-rich quartzites are characterized by thick granoblastic layers consisting of quartz ± albite (partially replaced by calcite), alternating with subordinate lepidoblastic layers composed of fine-grained white mica + chlorite + quartz. The definition of samples, either as quartzite or as mica-rich quartzite, mainly depends on the ratio between granoblastic and lepidoblastic layers. In both lithologies, the quartz-rich granoblastic layers are characterized by strong low-temperature (LT) dynamic recrystallization of the quartz grains, mainly through the subgrain rotation (SR) mechanism, and subordinately through the grain boundary migration (GBM) mechanism. Rare quartz porphyroclasts, affected by ductile intracrystalline deformation, are also preserved. The phyllosilicate-rich layers show the relationships between two different foliations (Figure 6a, b). The S1 continuous foliation, preserved inside the microlithons of the main foliation (S2), is highlighted by white mica + chlorite and by elongated quartz ± albite ribbons. By contrast, the S2 foliation is classifiable as a spaced to anastomosing crenulation cleavage, characterized by a discrete transition between the cleavage domains and the microlithons where the relics of the S1 foliation are preserved. The S2 foliation is outlined by aligned inequant fine-grained white mica + chlorite + quartz ± epidote and by thin layers of opaque minerals. In sample G26, euhedral fine-grained garnet porphyroblasts were also observed inside the S2 foliation domains (Figure 6c). They often include an older foliation (S1), arranged at high angle with respect to the main foliation (S2). C-type shear bands and asymmetric strain shadows showing a top-to-the-south shear sense occur around garnet porphyroblasts, with recrystallization of white mica + quartz + albite along the S2 foliation

Table 1. Selected metasedimentary rocks from the North Motagua fault zone (NMFZ)

Sample	Lithology	metamorphic assemblages													
		D1 phase					D2 phase								
		Qtz	Phe	Chl	Ab	Lws	Qtz	Phe	Chl	Grt	Ep	Bt	Stp	Amp	Ox
G12	Qtz-RICH MICASCHIST	*S1 not preserved*													
G13	Qtz-RICH MICASCHIST														
G24	Qtz-RICH MICASCHIST														
G25*	MICA-RICH QUARTZITE														
G26*	MICA-RICH QUARTZITE														
G40*	MICASCHIST														
G42*	MICASCHIST														
G52*	Qtz-RICH MICASCHIST														
G54	MICA-RICH QUARTZITE														
G55	QUARTZITE														

*Selected for electron microprobe analyses (EMPA).

DOI: 10.1002/gj

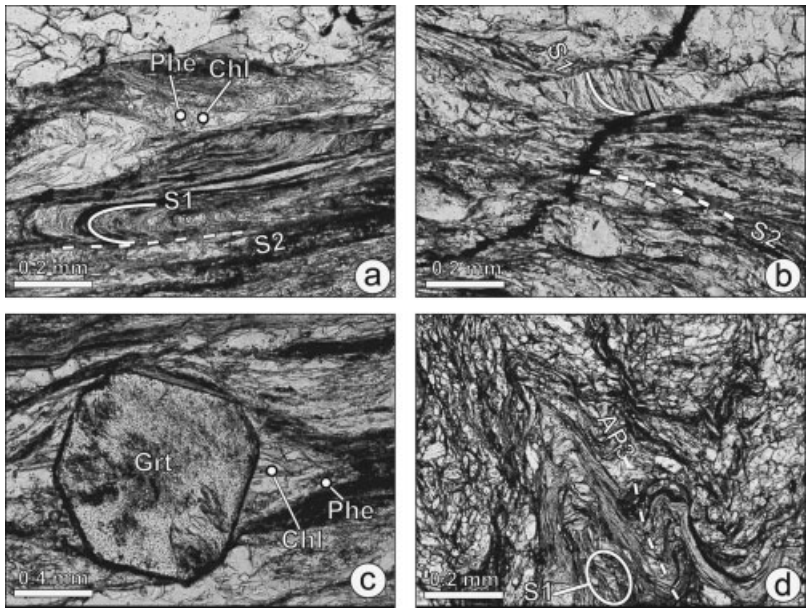

Figure 6. Photomicrographs of characteristic microstructures and mineral assemblages in the metasedimentary rocks from the North Motagua Fault Zone: (a–b) Relationship between S1 and S2 foliations in the mica-rich quartzites (sample G25); Chlorite (Chl) and phengite (Phe) aligned both along the S1 foliation preserved inside the microlithon and along the S2 foliation. Plane-polarized light; (c) Euhedral fine-grained garnet (Grt) porphyroblasts including an oldest foliation (S1), arranged at high angle with respect to the main S2 foliation (sample G26). Plane-polarized light and (d) S2 foliation deformed by close to isoclinal F3 micro-folds (sample G52). Plane-polarized light.

(Figure 6c). Finally, the S2 foliation is deformed by close to isoclinal F3 micro-folds. No growth of metamorphic minerals was observed associated with the F3 microfolds.

The quartz-rich micaschists are characterized by the irregular alternation of lepidoblastic layers composed of fine-grained phyllosilicates and thin granoblastic layers, mainly consisting of quartz, affected by strong LT dynamic recrystallization. Also, the quartz-rich micaschists are affected by a polyphased deformation and show the relationships between two different foliations. The S1 continuous foliation, preserved inside the microlithons of the main foliation (S2), is highlighted by white mica + chlorite + quartz ± albite ± lawsonite (Lws). By contrast, the S2 foliation is classifiable as a spaced to anastomosing crenulation cleavage, characterized by a discrete transition between the cleavage domains and the microlithons, where the relics of the S1 foliation are preserved. The S2 foliation is outlined by aligned fine-grained white mica + chlorite + quartz ± garnet ± epidote (Ep) ± stilpnomelane (Stp) and by thin layers of opaque minerals. Moreover, amphibole characterized by pale-green pleochroism was recognized only in sample G24. Close to isoclinal F3 micro-folds are present also in the quartz-rich micaschists (Figure 6d).

Discontinuous lepidoblastic layers of coarse-grained white mica, biotite and garnet characterize the micaschists. The garnet porphyroblasts are partially replaced by biotite + quartz ± white mica ± epidote aggregates. Moreover, granoblastic layers made up of quartz polycrystalline ribbons, affected by LT dynamic recrystallization (mainly through the SR mechanism), are also present. Rare coarse-grained quartz and K-feldspar porphyroclasts are preserved. The quartz porphyroclasts are affected by ductile LT intracrystalline deformation, whereas the feldspars are characterized by development of myrmekite along the grain boundaries, associated with albite exsolution lamellae. Quartz ribbons and aligned mica grains define a pervasive foliation (main foliation), recognizable also at the mesoscale. The main foliation is classifiable as a S2 foliation, because it preserves inside the microlithons an older S1 foliation, marked by folded white mica grains.

DOI: 10.1002/gj

4.3. Mineral chemistry

After a preliminary petrographic study, five samples (Table 1) were selected for mineral chemistry analysis. These samples include quartzites (G25 and G26), quartz-rich micaschists (G52) and micaschists (G40, G42). Coexisting minerals within the metamorphic assemblages have been analysed with a JEOL JXA-8600 electron microprobe (EMP), equipped with four wavelength-dispersive spectrometers, at the *CNR-Istituto di Geoscienze e Georisorse*, *Firenze*, Italy. Running conditions were 15 kV accelerating voltage and 10 nA beam current on a Faraday cage. Counting time for the determined elements ranged from 10 to 60 s at both peak and background. Nominal beam spot size was 1 μm for the analyses of all minerals, but alkali-rich minerals for which a defocused beam was employed to reduce the undesirable migration of volatile elements (from 5–15 μm in diameter according to grain size). Natural and synthetic silicates and oxides were used for instrumental calibration.

4.3.1. Phengite

All selected samples for EMP analyses include phengite in metamorphic mineral assemblages. Phengite structural formulae were calculated assuming 11 oxygen and all Fe as Fe^{2+}. If a small proportion of the Fe in phengite was Fe^{3+}, there would be a slight decrease in the Si content in the range of typically <0.1 atoms per formula unit (apfu) relative to the Fe^{3+}-free case. All analysed phengite has high celadonite contents as indicated by high Si, Mg and Fe (Table 2) relative to muscovite. Moreover, in many samples the small grain size of phengite also precluded any study of intracrystalline compositional variations (with the exception of sample G40), so that most analyses reported in Table 2 come from different crystals.

Table 2. Electron microprobe analyses of representative phengite

Sample	G25	G25	G25	G25	G25	G25	G26	G26	G26	G26	G26	G40	G40	G42	G42
Phengite	Phe3	Phe4	Phe6	Phe8	Phell	Phel2	Phel	Phe5	Phe7	Phe9	Phel0	Phe8	Phe11	Phe3	Phe7
Wt%															
SiO_2	49.67	49.33	49.80	50.71	50.99	50.74	48.47	49.91	50.21	50.18	49.68	49.73	50.61	49.55	49.58
TiO_2	0.08	0.16	0.42	0.16	0.10	0.08	0.13	0.13	0.10	0.10	0.19	0.48	0.61	0.33	0.38
Al_2O_3	28.23	28.19	27.81	27.97	27.38	27.82	27.27	29.76	27.92	28.75	29.23	27.80	26.98	28.56	29.29
Cr_2O_3	—	0.22	0.13	—	—	—	—	—	—	—	0.13	—	—	—	—
FeO	3.82	3.55	3.08	2.79	3.06	3.08	5.70	3.50	3.67	3.33	3.46	2.40	2.06	4.55	4.04
MnO	—	—	0.09	—	0.08	—	0.21	0.18	0.12	0 18	—	—	—	0.13	—
MgO	3.27	2.86	2.83	2.55	3.10	3.01	3.64	2.88	3.31	2.97	2.88	3.47	3.87	2.35	2.18
CaO	0.10	—	0.27	0.09	0.04	0.03	0.13	—	0.06	0.04	0.06	—	—	—	0.06
Na_2O	0.11	0.19	0.10	0.90	0.15	0.14	0.62	0.13	0.12	0.13	0.11	—	0.10	0.11	—
K_2O	9.91	10.23	10.16	9.91	10.15	10.32	8.55	10.35	10.07	10.35	10.29	10.62	10.82	10.46	10.71
Sum	95.19	94.73	94.69	95.08	95.05	95.22	94.72	96.84	95.58	96.03	96.03	94.5	95.05	96.04	96.24
Cations															
Si	3.33	3.33	3.36	3.39	3.41	3.39	3.29	3.29	3.35	3.34	3.30	3.35	3.39	3.32	3.30
Al^{IV}	0.67	0.67	0.64	0.61	0.59	0.61	0.71	0.71	0.65	0.66	0.70	0.65	0.61	0.68	0.70
Al^{VI}	1.56	1.57	1.56	1.59	1.57	1.58	1.48	1.61	1.55	1.59	1.60	1.56	1.52	1.57	1.61
Ti	0.00	0.01	0.02	0.01	0.01	0.00	0.01	0.01	0.01	0.00	0.01	0.02	0.03	0.02	0.02
Cr	0.00	0.01	0.01	0.00	0.00	0.00	0.00	0.00	0.01	0.00	0.01	0.00	0.00	0.00	0.00
Fe	0.21	0.20	0.17	0.16	0.17	0.17	0.32	0.19	0.20	0.19	0.19	0.14	0.12	0.25	0.23
Mn	0.00	0.00	0.01	0.00	0.00	0.00	0.01	0.01	0.01	0.01	0.00	0.00	0.00	0.01	0.00
Mg	0.33	0.29	0.28	0.25	0.31	0.30	0.37	0.28	0.33	0.29	0.29	0.35	0.39	0.23	0.22
Ca	0.01	0.00	0.02	0.01	0.00	0.00	0.01	0.00	0.00	0.00	0.00	0.00	0.00	0.00	0.00
Na	0.01	0.02	0.01	0.12	0.02	0.02	0.08	0.02	0.02	0.02	0.01	0.00	0.01	0.01	0.00
K	0.85	0.88	0.87	0.84	0.87	0.88	0.74	0.87	0.86	0.88	0.87	0.91	0.92	0.89	0.91
Sum	6.98	6.99	6.96	6.98	6.95	6.96	7.02	6.99	6.98	6.98	6.98	6.98	6.99	6.99	6.98

— : below detection limits.

DOI: 10.1002/gj

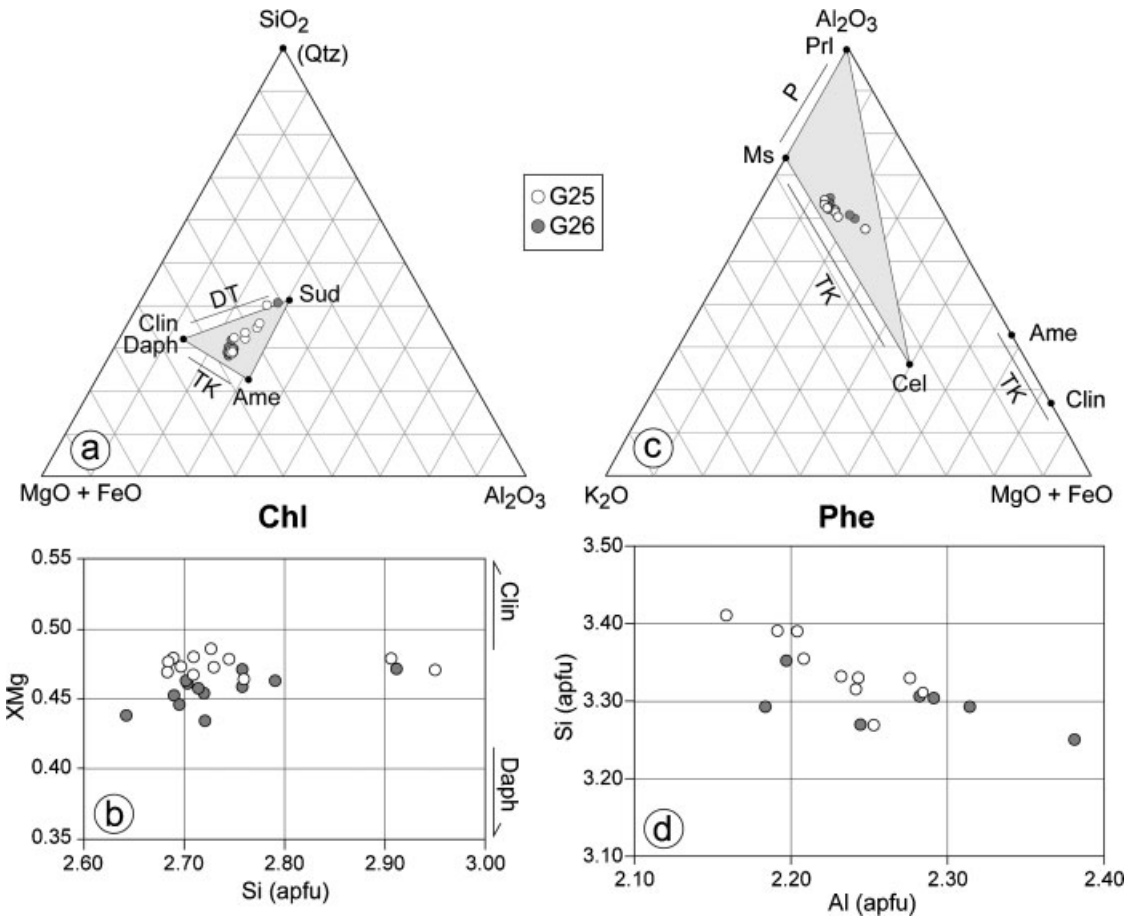

Figure 7. Compositional variability of chlorite (a–b) and phengite (c–d) from the selected samples for thermodynamic calculations (G25 and G26): (a) SiO_2-Al_2O_3-(MgO+FeO) ternary diagram; (b) Si (apfu) versus XMg diagram; (c) Al_2O_3-(MgO+FeO)-K_2O ternary diagram and (d) Al (apfu) versus Si (apfu) diagram. Abbreviations: Clin: clinochlore; Daph: daphnite; Ame: (Fe, Mg)-amesite; Sud: (Fe, Mg)-sudoite; Cel: (Fe, Mg)-celadonite; Ms: muscovite; Prl: pyrophyllite; TK: Tschermak substitution; DT: di/trioctahedral substitution; P: pyrophyllitic substitution.

The analysed phengite from the quartzites (G25, G26) is aligned both along the S1 foliation preserved inside the microlithons and along the S2 foliation (main foliation). Phengite from these samples has Si contents between 3.24 and 3.41 apfu (Figure 7). The analysed phengite from the micaschists (G40, G42) is mainly aligned along the main foliation (S2). The coarse-grained phengite crystals from the sample G40 show core-to-rim variation in chemical composition, i.e. the cores have higher Si contents (3.31–3.39 apfu) in comparison with the rims (3.19–3.24 apfu). Phengite from sample G42 has Si contents ranging between 3.16 and 3.32 apfu.

4.3.2. Chlorite

For the analysed chlorite, structural formulae were calculated assuming 14 oxygen (Table 3). In the structural formulae from Table 3, the Fe content is shown as divalent (Fe_{tot}). As well as for the phengite, the analysed chlorite from the quartzites (G25, G26) and quartz-rich micaschists (G52) is aligned both along the S1 foliation preserved inside the microlithons and along the S2 foliation (main foliation). It has Si contents between 2.64 and 3.07 apfu and $Mg/(Mg + Fe^{2+} + Mn)$ ratios ranging from 0.43 to 0.49 (Figure 7), with the exception of chlorite from sample G52 that shows higher $Mg/(Mg + Fe^{2+} + Mn)$ ratios (0.69–0.70).

DOI: 10.1002/gj

Table 3. Electron microprobe analyses of representative chlorite

Sample	G25	G25	G25	G25	G25	G25	G26	G26	G26	G26	G26	G52	G52
Chlorite	Chl3	Chl6	Chl8	Chl12	Chl15	Chl16	Chl2	Chl5	Chl6	Chl9	Chl10	Chl2	Chl5
Wt%													
SiO_2	28.37	25.67	26.30	26.21	25.77	25.78	25.68	27.28	25.57	24.87	25.62	27.80	28.12
TiO_2	0.06	0.11	0.08	—	—	—	—	0.05	—	—	—	—	—
Al_2O_3	22.31	21.66	21.65	20.96	21.23	21.49	21.55	20.88	21.59	21.27	20.65	21.24	21.14
Cr_2O_3	0.07	0.11	—	—	—	—	—	—	0.09	—	—	0.13	0.17
FeO	23.95	26.56	26.84	27.16	27.44	26.59	26.98	27.87	27.60	28.50	27.74	16.07	17.05
MnO	0.80	0.66	0.83	0.74	0.73	0.64	1.15	1.12	1.02	1.37	1.10	0.16	0.26
MgO	12.78	14.09	13.95	13.58	13.89	14.13	13.53	14.05	13.30	13.10	13.68	21.55	22.03
CaO	—	0.07	0.05	0.08	0.00	0.00	0.00	0.13	0.07	0.07	0.00	0.07	0.06
Na_2O	—	—	—	—	—	—	—	0.12	—	—	—	—	—
K_2O	1.12	0.07	0.11	—	—	—	—	0.05	—	0.03	0.08	0.03	0.03
Sum	89.46	89.00	89.81	88.73	89.06	88.63	88.89	91.55	89.24	89.21	88.87	87.05	88.86
Cations													
Si	2.90	2.69	2.73	2.76	2.71	2.71	2.70	2.79	2.69	2.64	2.71	2.80	2.79
Al^{IV}	1.10	1.31	1.27	1.24	1.29	1.29	1.30	1.21	1.31	1.36	1.29	1.20	1.21
$A1^{VI}$	1.59	1.36	1.37	1.35	1.33	1.36	1.37	1.30	1.36	1.30	1.29	1.32	1.26
Ti	0.00	0.01	0.01	0.00	0.00	0.00	0.00	0.00	0.00	0.00	0.00	0.00	0.00
Cr	0.01	0.01	0.00	0.00	0.00	0.00	0.00	0.00	0.01	0.00	0.00	0.01	0.01
Fe	2.05	2.32	2.33	2.39	2.41	2.33	2.37	2.38	2.42	2.53	2.45	1.35	1.41
Mn	0.07	0.06	0.07	0.07	0.06	0.06	0.10	0.10	0.09	0.12	0.10	0.01	0.02
Mg	1.95	2.20	2.15	2.13	2.17	2.21	2.12	2.14	2.08	2.07	2.16	3.23	3.25
Ca	0.00	0.01	0.01	0.01	0.00	0.00	0.00	0.01	0.01	0.01	0.00	0.01	0.01
Na	0.00	0.00	0.00	0.00	0.00	0.00	0.00	0.02	0.00	0.00	0.00	0.00	0.00
K	0.15	0.01	0.01	0.00	0.00	0.00	0.00	0.01	0.00	0.00	0.01	0.00	0.00
Sum	9.82	9.97	9.95	9.94	9.98	9.96	9.96	9.97	9.97	10.03	10.01	9.94	9.97

—: below detection limits.

4.3.3. Biotite

Only the micaschist samples (G40, G42) include biotite in the metamorphic mineral assemblage. For the analysed biotite structural formulae were calculated assuming 11 oxygen and all Fe have been treated as Fe^{2+} (Table 4). The biotite belonging to sample G40 shows X_{Mg} ratio ($Mg/(Mg + Fe^{2+})$) ranging from 0.66 to 0.72. The biotite from sample G42 has higher Fe contents (23.10–24.57 Wt%), so it has lower X_{Mg} (0.33–0.37).

4.3.4. Garnet

Garnet porphyroblasts belonging to the sample G26 were analysed. Garnet structural formulae were calculated assuming 24 oxygen and all Fe as Fe^{2+} (Table 5 and Figure 8). They show a chemical zoning and are characterized by cores rich in the grossular (Grs) component, with moderate spessartine (Sps) and almandine (Alm) ($Grs_{43.3\text{-}45.2}$ $Sps_{36.8\text{-}39.3}$ $Alm_{16.9\text{-}17.4}$ $Pyr_{0.5\text{-}0.6}$). By contrast, the rims are rich Sps component, with moderate Grs and Alm ($Sps_{41.4\text{-}44.8}$ $Grs_{30.1\text{-}33.8}$ $Alm_{22.5\text{-}27.5}$ $Pyr_{0.5\text{-}1.0}$). The X_{Mg} ratio, ranging between 0.02 and 0.04, is quite homogeneous in both core and rim. On the whole, the analysed garnet shows from core to rim an increase of Sps component and a decrease of the Grs component. This feature implies a progressive decrease of temperature during the growth of garnet porphyroblasts (e.g. Sakai *et al*. 1985; Banno *et al*. 1986; Enami 1998).

4.3.5. Other minerals

All analysed albite, which structural formulae were calculated assuming 8 oxygen, has compositions close to the pure end-member. For K-feldspar porphyroclasts, structural formulae were calculated assuming 8 oxygen. The K-

DOI: 10.1002/gj

Table 4. Electron microprobe analyses of representative biotite

Sample	G40	G40	G40	G40	G42	G42
Biotite	Bt1	Bt2	Bt4	Bt5	Bt3	Bt4
Wt%						
SiO_2	38.27	39.94	40.06	40.26	36.20	36.09
TiO_2	1.19	1.49	1.30	1.42	1.98	2.32
Al_2O_3	17.17	17.74	18.47	18.23	17.76	17.23
Cr_2O_3	—	—	—	—	—	—
FeO	12.31	11.08	10.17	10.99	23.19	24.57
MnO	0.13	0.14	—	0.22	0.68	0.60
MgO	13.53	14.97	14.87	14.28	6.97	6.82
CaO	0.18	0.10	0.13	0.06	—	0.05
Na_2O	—	0.11	—	—	—	—
K_2O	8.65	8.83	8.93	9.11	9.02	9.25
Sum	91.43	94.4	93.93	94.57	95.8	96.93
Cations						
Si	2.90	2.91	2.91	2.93	2.79	2.77
Al^{IV}	1.10	1.09	1.09	1.07	1.21	1.23
Al^{VI}	0.44	0.43	0.50	0.49	0.40	0.33
Ti	0.07	0.08	0.07	0.08	0.11	0.13
Cr	0.00	0.00	0.00	0.00	0.00	0.00
Fe	0.78	0.67	0.62	0.67	1.49	1.58
Mn	0.01	0.01	0.00	0.01	0.04	0.04
Mg	1.53	1.62	1.61	1.55	0.80	0.78
Ca	0.01	0.01	0.01	0.00	0.00	0.00
Na	0.00	0.02	0.00	0.00	0.00	0.00
K	0.84	0.82	0.83	0.84	0.89	0.91
Sum	7.68	7.67	7.64	7.64	7.74	7.77

—: below detection limits.

feldspar from all analysed samples has a composition close to the orthoclase end-member, with minor amounts of Na.

4.4. Estimation of metamorphic pressure–temperature (P–T) conditions

In the NMFZ, the metaophiolites are represented by several blocks of eclogite and jadeitite set in a mainly metasedimentary matrix. The eclogites are represented by paragonite-bearing zoisite eclogite, characterized by the following peak metamorphism assemblage: Grt + Omp + Zo + Phe (3.50 Si apfu) + Pg + Rt + Qtz. The relative P–T conditions were estimated as 2.00–2.30 GPa and 600–650°C (Tsujimori *et al*. 2004). Moreover, these rocks were overprinted by amphibolite-facies mineral assemblage with new growth of garnet during decompression, and then overprinted by blueschist-facies minerals (Tsujimori *et al*. 2004). In turn, the jadeitites consists mostly of jadeite (Jd), with minor Omp + Phe and/or Pg + Ab + Ttn. Conditions of jadeitites formation are 100–400°C and 0.50–1.10 GPa (Harlow 1994).

In this work, the investigated samples consist of rocks belonging to the metasedimentary matrix (quartzite, quartz-rich micaschist, micaschist) (Table 1). Two different foliations (referred to as S1 and S2) were observed in all the studied rocks. The metamorphic assemblage associated with the S1 foliation is made up of Phe + Chl + Qtz ± Ab in the quartzite, Phe + Chl + Qtz ± Ab ± Lws in the quartz-rich micaschists and Phe in the micaschists. By contrast, the S2-related assemblage is composed of Phe + Chl + Qtz ± Grt ± Ep in the quartzites, Phe + Chl + Qtz ± Grt ± Ep ± Stp ± Amp in the quartz-rich micaschists and Phe + Bt + Qtz ± Grt in the micaschists.

DOI: 10.1002/gj

Table 5. Electron microprobe analyses of representative garnet

Sample	G26	G26	G26	G26	G26	G26
Garnet	Grtl_c	Grtl_r	Grt4_c	Grt4_r	Grt6_r	Grt8_r
Wt%						
SiO_2	37.78	38.16	37.41	38.61	37.85	36.76
TiO_2	1.98	0.11	2.76	0.00	0.11	1.93
Al_2O_3	20.70	21.93	20.01	22.23	21.94	20.68
Cr_2O_3	—	—	—	—	—	—
FeO	7.70	11.85	7.65	13.89	10.54	10.41
MnO	16.13	19.60	17.56	18.48	20.61	19.70
MgO	0.14	0.22	0.12	0.20	0.26	0.13
CaO	15.66	10.85	15.28	11.25	11.53	12.18
Na_2O	—	0.15	—	—	—	—
K_2O	—	—	—	—	0.03	—
Sum	100.09	102.87	100.79	104.66	102.87	101.79
Cations						
Si	5.96	5.96	5.90	5.93	5.91	5.82
Al	3.85	4.04	3.72	4.03	4.04	3.86
Ti	0.23	0.01	0.33	0.00	0.01	0.23
Fe	1.02	1.55	1.01	1.79	1.38	1.38
Mn	2.15	2.59	2.35	2.41	2.73	2.64
Mg	0.03	0.05	0.03	0.05	0.06	0.03
Ca	2.65	1.81	2.58	1.85	1.93	2.07
Sum	15.89	16.01	15.91	16.05	16.06	16.02
Pyr	0.56	0.85	0.47	0.75	0.99	0.50
Alm	17.36	25.76	16.92	29.32	22.59	22.53
Grs	45.24	30.22	43.29	30.42	31.67	33.78
Sps	36.84	43.16	39.33	39.51	44.75	43.19

—: below detection limits.
c: core; r: rim; Pyr: Pyrope; Alm: Almandine; Grs: Grossular; Sps: Spessartine.

Two samples (G25, G26) of quartzite, characterized by thick phyllosilicate-rich lepidoblastic layers (mica-rich quartzite), were selected for the thermodynamic calculations in order to estimate the P–T evolution of the metamorphism in the metasedimentary matrix. In these samples, both the observed foliations are characterized by the growth of Phe + Chl + Qtz. Vidal and Parra (2000) showed that in low- to medium-grade metapelites, chlorite-

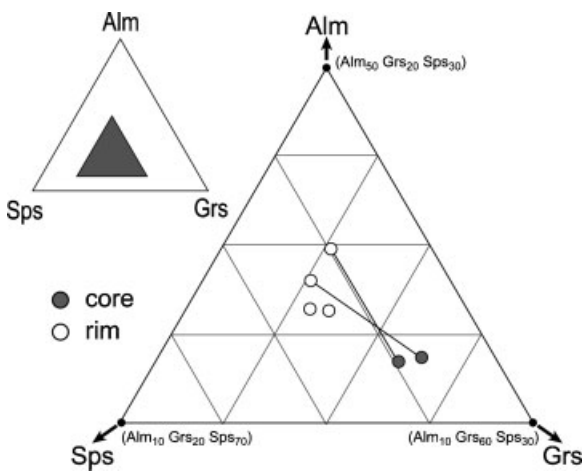

Figure 8. Compositional variability of garnet from sample G26 on the Alm-Grs-Sps ternary diagram.

DOI: 10.1002/gj

phengite local equilibria can be used to constrain the P–T evolution of exhumed high-pressure rocks. The concept of local equilibrium is consistent with the observed chemical variability among different grains of the same phase coexisting in the same thin section. This reflects the lack of equilibrium at distances above a few millimetres, and the coexistence of several mineral generations that did not totally re-equilibrate during the metamorphic P–T evolution. The technique of chlorite-phengite multi-equilibrium calculation, based on the assumption of local equilibrium, has been used recently by many authors (e.g. Trotet *et al.* 2001a,b; Parra *et al.* 2002b; Augier *et al*. 2005; Rimmelé *et al*. 2005; Willner 2005; Malasoma and Marroni 2007).

Here this method was used to constrain the P–T conditions of metamorphism in the metasedimentary rocks. In samples G25 and G26 several chlorite-phengite pairs, both on the S1 foliation preserved inside the microlithons and on the S2 foliation (main foliation), were analysed. The chlorite-phengite pairs used to perform the thermodynamic calculations were first selected using classical textural criteria suggesting equilibrium (e.g. minerals in contact, no evidence of reaction, grown in the same microstructure). A further selection of the analyses was made on the basis of the chemical criteria aimed at rejecting mineral compositions that do not form a linear combination of the end-members used in the chlorite and white mica solid-solution models. The thermodynamic calculations used in the present study are performed with TWEEQ software (Berman 1991). The thermodynamic data and the solid-solution models are from Berman (1988; 1990) for all phases except K-white mica and chlorite, for which the models of Parra *et al.* (2002a) and Vidal *et al.* (2001, 2005) were used, respectively. The end-members to use for the thermodynamic calculations, should describe the white mica and chlorite chemical composition. For the white mica, the following end-members were used: Mg-Al-celadonite $(\text{Mg-ACel})_{\text{Phe}}$, Fe-Al-celadonite $(\text{Fe-ACel})_{\text{Phe}}$, pyrophyllite $(\text{Prl})_{\text{Phe}}$ and muscovite $(\text{Ms})_{\text{Phe}}$, whereas for the analysed chlorites, characterized by high Si contents, we used 3 end-members: Mg-sudoite $(\text{Sud})_{\text{Chl}}$, clinochlore $(\text{Clin})_{\text{Chl}}$ and daphnite $(\text{Daph})_{\text{Chl}}$. The presence of Fe^{3+} will affect the activity of chlorite end-members, although it is generally neglected because no difference can be made between Fe^{2+} and Fe^{3+} with the microprobe. An estimation of Fe^{3+} in chlorite can be done using the criterion proposed by Vidal *et al*. (2006).

The number of reactions that can be computed for a given paragenesis involving chlorite and phengite, depends on the number of end-members used to express the compositional variability of these minerals. As shown in Figure 9, in the K_2O-Al_2O_3–FeO–MgO-SiO_2-H_2O system, the P–T conditions for the chlorite-phengite-quartz-H_2O assemblage are given by the intersection of 13 equilibria, among which three are independent. Some scatter of the intersection points in the diagrams was observed. According to Vidal and Parra (2000), this scatter results from cumulated errors in each reaction, which stem from the uncertainties in the thermodynamic standard-state properties of the end-members and the solution models, departure of the analysed compositions from equilibrium compositions and analytical uncertainties. The first source of error, resulting from the uncertainties associated with the thermodynamic data, is difficult to estimate because the thermodynamic standard-state properties were calibrated using experimental and natural data of various levels of confidence. However, it is likely that the uncertainties in the thermodynamic data have a systematic effect on the calculated locations of the intersection points, but not on their relative positions. Finally, even if the thermodynamic data were 'perfect', imprecision on the analysed compositions places limits on the precision with which P–T can be estimated.

The average P–T estimates and their associated deviations (σP and σT) were calculated for each mineral pair by the INTERSX software included in the TWEEQ package (Berman 1991). According to Berman (1991), Vidal and Parra (2000), Trotet *et al*. (2001a) and Parra *et al*. (2002b), the magnitude of the pressure (σP) and temperature (σT) scatter for the calculated equilibria lead to reject the chlorite–phengite pairs, which are considered to be out of equilibrium. Assuming that the thermodynamic data are 'perfect' and equilibrium is achieved, the scatter resulting from analytical uncertainties is given by the precision of the microprobe analysis. It can be calculated with a Monte Carlo technique (Lieberman and Petrakakis 1991; Vidal and Parra 2000), which lead to the estimation of the maximum permissible scatter (σP_{max} and σT_{max}) of any P–T estimate. The estimated σP_{max} and σT_{max} values for assemblages including chlorite and phengite are 0.08 GPa and 25°C, respectively (Vidal and Parra 2000; Trotet *et al*. 2001a; Parra *et al*. 2002b; Augier *et al*. 2005; Rimmelé *et al*. 2005).

Calculated Chl-Phe-Qtz-H_2O equilibrium P–T conditions using different chlorite-phengite pairs from the samples G25 and G26 are shown in Figure 10. If $\sigma P > 0.08$ GPa and/or $\sigma T > 25$°C the assemblages are considered

DOI: 10.1002/gj

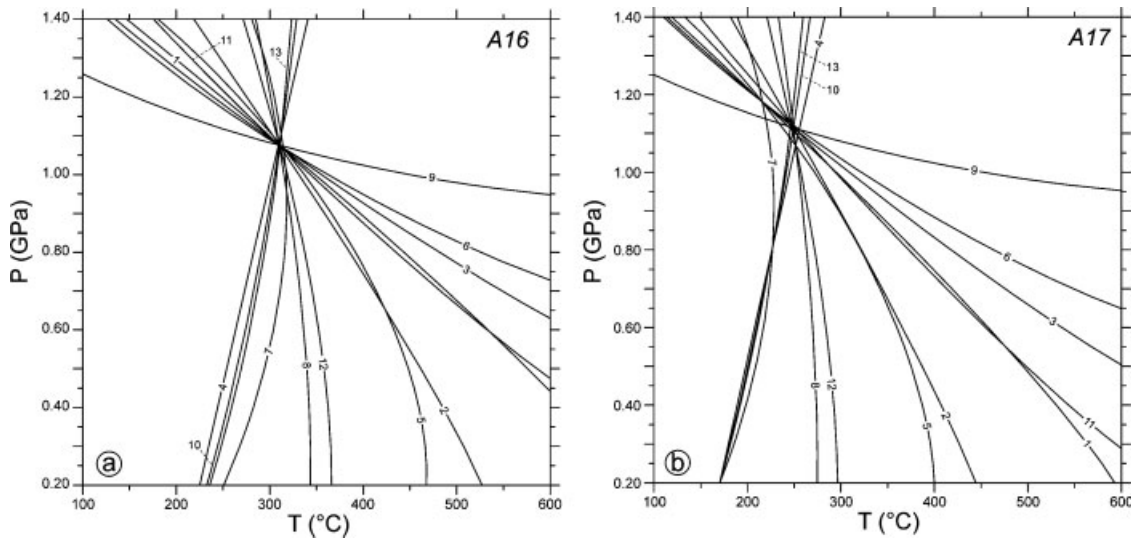

Figure 9. Examples of P–T plot of chlorite-phengite-quartz-H_2O local equilibrium for two different Phe-Chl pairs from sample G25. See text for explanations about the used solid-solution models and end-members. Reaction curves: 1: 8 Prl + 10 MgACel + 2 Daph + 4 W = 5 Sud + 10 FeACel + 23 Qtz; 2: 8 Prl + 2 Clin + 4 W = 5 Sud + 23 Qtz; 3: 2 MgACel + 4 Prl = 15 Qtz + 2 Ms + Sud; 4: Daph + 5 MgACel = 5 FeACel + Clin; 5: 14 Prl + 23 Ms + 52 MgACel + 15 Daph + 30 W = 26 Sud + 75 FeACel; 6: 5 FeACel + 6 Prl = 26 Qtz + 5 Ms + Daph + 2 W; + 2 W; 7: 3 Sud + 10 FeACel = 7 Qtz + 4 Ms + 6 MgACel + 2 Daph + 4 W; 8: 14 Prl + 23 Ms + 15 Clin + 30 W = 26 Sud + 23 MgACel; 9: 5 MgACel + 6 Prl = 26 Qtz + 5 Ms + Clin + 2 W; 10: 3 Sud + 4 MgACel = 7 Qtz + 4 Ms + 2 Clin + 4 W; 11: 2 Clin + 10 FeACel + 20 Prl = 75 Qtz + 10 Ms + 2 Daph + 5 Sud; 12: 70 Prl + 115 Ms + 52 Clin + 23 Daph + 150 W = 130 Sud + 115 FeACel; 13: 15 Sud + 20 FeACel = 35 Qtz + 20 Ms + 6 Clin + 4 Daph + 20 W.

to be out of equilibrium and the P–T estimates are rejected. A significant proportion of the Chl–Phe pairs can be considered in equilibrium, so they can be used for the P–T estimations. The P–T points constrained by the composition of selected chlorite-phengite pairs define a continuous trend in the diagram, characterized by temperatures ranging from 206 to 409°C and pressures ranging from 1.25 to 0.70 GPa (Figure 10). Moreover, the calculated points are arranged in two main clusters (well recognizable in the data from sample G26), mainly characterized by different temperature conditions. Most of the analysed Chl-Phe pairs along the S2 foliation (main foliation) show a maximum clustering at 279–409°C (with pressures ranging from 1.20 to 0.70 GPa), while the analysed Chl-Phe pairs inside the microlithons (S1 foliation) display lower T conditions (206–263°C) and slightly higher P conditions (1.25–1.00 GPa). Summing up the available data from the thermodynamic calculations, the first part of the inferred P–T path is characterized by a very LT metamorphic gradient (~5–8°C km^{-1}). Moreover, the P–T trajectory is characterized by a first increase of the T conditions (of ~100–150°C), followed by a segment in which the P decreasing (of ~0.40–0.50 GPa) is associated to a slightly decrease of T. Therefore, the continuous trend shown by the points in the P–T diagram (Figure 10), that can be regarded as part of the metamorphic evolution of the NMFZ metasedimentary matrix, probably defines a part of the exhumation path of these rocks from the lawsonite blueschist facies (D1 phase) to lower P and higher T conditions (low-grade epidote blueschist facies, D2 phase).

In sample G26, the D2 phase mineral assemblage is also characterized by the presence of the garnet porphyroblasts. The analysed garnet, showing a core-to-rim chemical zonation, is characterized by a high content in Mn (spessartine component). Moreover, also the bulk chemical composition of the selected quartzites is probably characterized by a high Mn content, considering that they derived from the pelagic sedimentary cover (metaradiolarite) of the ophiolitic sequence. Calculations based on a KMnFMASH petrogenetic grid derived using an internally consistent thermodynamic dataset indicate that the principal effect of the presence of Mn in average subaluminous pelite compositions is to stabilize garnet to higher and lower pressures and temperatures over a wide

DOI: 10.1002/gj

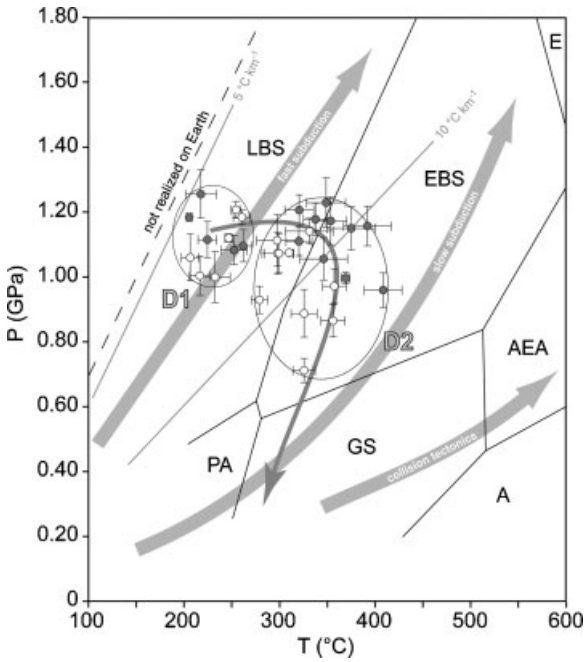

Figure 10. Estimated metamorphic P–T conditions in the NMFZ metasedimentary rocks. Calculated Chl-Phe-Qtz-H_2O equilibrium P–T conditions using different Phe-Chl pairs (local equilibria method of Vidal and Parra 2000) from samples G25 (white circles) and G26 (grey circles). The average P–T estimates and the scatter of intersection (σT and σP) were calculated using INTERSX software (Berman 1991). Stability field of the metamorphic facies are from Evans (1990). Abbreviations: A: amphibolite facies; AEA: albite-epidote-amphibolite facies; E: eclogite facies; EBS: epidote blueschist facies; GS: greenschist facies; LBS: lawsonite blueschist facies and PA: pumpellyite-actinolite facies.

range of bulk compositions. Therefore, since an addition of Mn will expand the garnet-bearing field to lower temperatures and pressures, garnet might be stable and represent an extra phase at lower temperature and pressure conditions than in a Mn-free system (Spear and Cheney 1989; Symmes and Ferry 1992; Mahar *et al*. 1997; Wei *et al*. 2004). In particular, the predicted temperature of the garnet-in isograd (~450°C, according to Bucher and Frey 2002) is lowered by as much as 100°C by the addition of Mn to KFMASH. These predicted P–T conditions are consistent with those estimated for the D2 phase using the Phe-Chl local equilibria method (0.70–1.20 GPa and 279–409°C). Moreover, the chemical zoning recognized in the analysed porphyroblasts is coherent with a progressive decrease of T during their growth, maybe occurred during the last segment of the estimated P–T path, from the D2 metamorphism to lower grade conditions (Figure 10).

The metamorphic mineral assemblages recognized in the other lithologies belonging to the metasedimentary matrix, are consistent with the metamorphic history proposed for the selected quartzites (samples G25, G26). Particularly, the D1 assemblages are characterized by the presence of Si-rich phengite and lawsonite; by contrast, the D2 assemblages record an increase of the T conditions, as testified by the growth of garnet and epidote in the S2 foliation domains. The presence of biotite in the micaschists is consistent with higher T conditions (the first prograde biotite appears at about 420°C, according to Bucher and Frey 2002), if compared with those estimated for the quartzites.

5. DISCUSSION

The deformations shown by the metasedimentary rocks from NMFZ provide evidences of a complex history, acquired during its displacement from very deep structural levels up to the surface in the framework of a subduction

DOI: 10.1002/gj

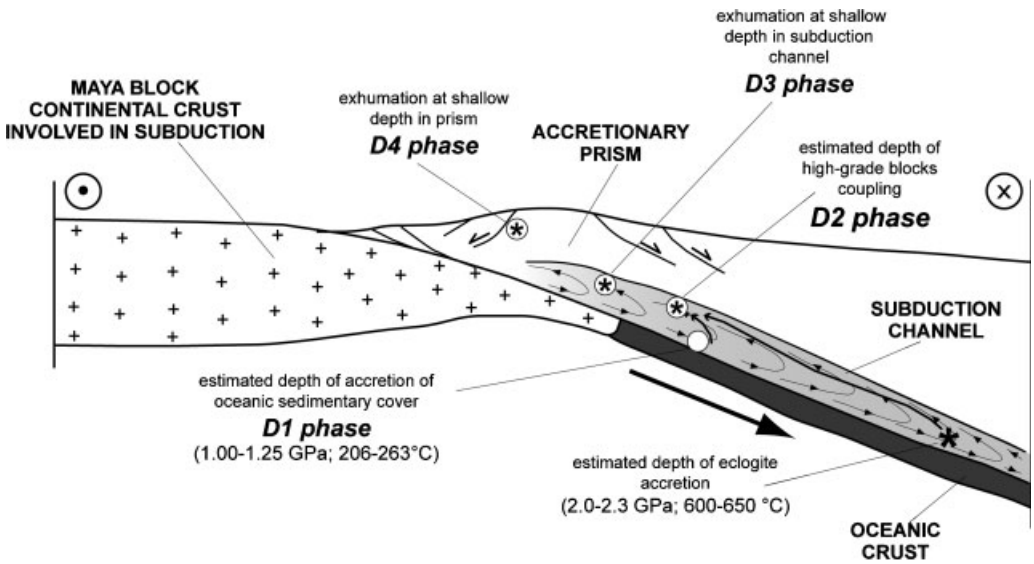

Figure 11. Schematic reconstruction of blocks and matrix evolution in the subduction channel (not to scale). The estimated metamorphic climax (i.e. depth of accretion) of different mélange components, as well as a proposed setting of high-grade blocks coupling, are shown (P–T estimation for eclogites from Tsujimori *et al*. 2004).

complex located from Cretaceous to Tertiary at the northern border of the Caribbean Plate (Figure 11). This deformation history is able to provide some valuable insights for the reconstruction of the tectonic processes active in a subduction complex. The fundamental points will be separately discussed in the following paragraphs.

5.1. The D1 phase as the remnant of the accretion process?

The metasedimentary rocks from the NMFZ mélange display evidences of a relic S1 foliation, recognized in the microlithons wrapped by the S2 foliation. The very poor remnants of the D1 phase, that is detected mainly in thin section, hampers any clear statement about its process of origin. However, some insights can be derived from the features of the S1 foliation, that can be described as a schistosity characterized by the growth of phengite + chlorite + quartz ± albite ± lawsonite. The estimated metamorphic conditions for the D1 phase in the quartzites, determined by using the chlorite-phengite local equilibria method, indicate a T ranging from 206 to 263°C with a P ranging from 1.00 to 1.25 GPa. These conditions can be referred to a cold geothermal gradient of about 5–8°C km^{-1}, as that postulated for the subduction where cold oceanic crust is involved (e.g. Peacock and Wang 1999; Tsujimori *et al*. 2006a and quoted references). This geothermal gradient can be compared with the P–T conditions estimated for the eclogites from the SMFZ (Harlow *et al*. 2003; Tsujimori *et al*. 2005; Tsujimori *et al*. 2006b). In these rocks the inferred P–T trajectory lies near a geothermal gradient of 5°C km^{-1}, that can be compared with the thermal structure of some active subduction zones, as for instance the NE Japan zone (Peacock and Wang 1999), or fossil accretionary wedges, e.g. the Samanà Peninsula from the Dominican Republic (e.g. Zack *et al*. 2004), the Farallon Plate from the Colorado Plateau (e.g. Usui *et al*. 2003), the Ward Creek from the Franciscan Complex (e.g. Shibakusa and Maekawa 1997) and the North Qilian Suture Zone from China (e.g. Song *et al*. 2007). In all these fossil examples, the climax of the HP metamorphism is interpreted as related to the underplating of slices of oceanic lithosphere at the base of the accretionary wedge. If this interpretation is also proposed for the D1 phase recognized in the metasedimentary rocks from the NMFZ mélange (Figure 11), the related relics can be regarded as the remnants of an underplating process developed in an intraoceanic subduction setting.

DOI: 10.1002/gj

5.2. The geodynamic interpretation of the post-D1 phases

The microstructural observations and mineral chemistry data presented in this study show that the transition from the D1 to the D2 phase was characterized by the continuous growth of several generations of phengite-chlorite pairs in the mica-rich quartzites. The mineral chemistry of these pairs indicate that the P–T conditions change from 1.00–1.25 GPa and 206–263°C, for the D1 phase, to 0.70–1.20 GPa and 279–409 °C for the D2 phase. In the other lithologies, the D2 metamorphic mineral assemblages are characterized by the growth of garnet, epidote and biotite. So, the transition from D1 to D2 seems to record a slightly decompressional path associated with a strong heating. In addition, the comparison between the deformations of the D2 phase with those of the following D3 and D4 ones indicates that the latter two developed at a shallower depth, as pointed out by the features of the foliation or the associated synkinematic recrystallizations. On the whole, the post-D1 phases can be interpreted as the record of deformations developed during the progressive transition of the NMFZ mélange from deep to superficial structural levels. In addition, the P–T conditions determined for the D2 phase indicate its development in a geodynamic setting characterized by a warm geothermal gradient, different from that established for the D1 phase. Temperatures at depth in a subduction zone depend on many parameters including the thermal structure of the incoming lithosphere, convergence rate, geometry of the subduction zone, radioactive heating and rates of shear heating along the subduction shear zone (Peacock 1996; Peacock and Wang 1999). According to the geodynamic constraints, the transition from D1 to D2 phase can be interpreted as the record of a change in the active geodynamic process, from intraoceanic subduction to inception of continental collision. Summing up these observations, the post-D1 phases can be regarded as being related to progressive exhumation of the NMFZ mélange during the continental collision developed after the intraoceanic subduction.

5.3. The mechanism of the exhumation: the D2 and D3 phase

The deformation features of the D2, D3 and D4 phases reconstructed in the metasedimentary rocks from the NMFZ mélange provides some insights for the understanding of its exhumation history. In particular, these phases show great differences in their structural features, suggesting that the exhumation of the mélange was probably achieved by different mechanisms active at different times. The D2 one, characterized by isoclinal folds with strongly thinned or boudinaged limbs, pervasive foliation parallel to the lithological layers and well-developed mineral/stretching lineation represent the first exhumation-related deformation. All these features are indicative of a deformation similar to that recognized during crustal shortening. This type of deformation has been described in many subducted continental-derived units. To explain these deformation mechanisms, developed during the exhumation processes, several authors (e.g. Chemenda *et al*. 1995, 1996, 2000; Thompson *et al*. 1997a; Ernst 1999) proposed the extrusion model. This model suggests that the HP-metamorphic rocks, when detached from subducting continental lithosphere, may be exhumed by buoyancy forces as tectonic slices bounded by a normal fault at the top and a thrust at the base. This model considers the uplift to upper structural levels of relatively thick and coherent units derived from continental lithosphere. By contrast, in the case of the NMFZ rocks, the extrusion of high-grade blocks embedded in a matrix, i.e. a tectonic mélange, seems to be the most suitable exhumation mechanism. Extrusion through mélange formation has been proposed in the framework of the subduction channel model (Cloos 1982; Cloos and Shreve 1988; Platt 1986, 1993; Allemand and Lardeaux 1997; Schwartz *et al*. 2001; Gerya *et al*. 2002; Gorczyk *et al*. 2007). In the subduction channel, i.e. the shear zone located between the descending plate and the accretionary wedge, the oceanic material is generally not only transported down by underthrusting, but also translated upward by return-flow back to the surface. At depths less than 50 km, hydrated sediments can easily lubricate the interface between the two plates to facilitate exhumation of blocks of HP-metamorphic rocks greater than hundreds of metres in size embedded in a low-density matrix, as documented in the Franciscan Complex (Cloos 1982; Cloos and Shreve 1988; Platt 1986) and in the Northern Serpentinite Mélange from Cuba and Hispaniola islands (e.g. Gorczyk *et al*. 2007). The same features are recognized in the NMFZ mélange, where blocks of the relatively dense rocks as the eclogites, imbedded in a low-density metasedimentary and/or metaserpentinitic matrix, seem to be a suitable material to be subjected to buoyancy forces in a subduction

DOI: 10.1002/gj

channel. Moreover, the trend of the mineral/stretching lineation (L2), characterized by a dominant strike-slip component (parallel to the trend of the suture zone), suggests that the extrusion was largely controlled by strike-slip tectonics which occurred between the Maya and Chortis microplates. This fits with the geodynamic reconstructions of the Carribbean Plate (e.g. Dengo 1985; Burke 1988; Pindell *et al*. 1988; Pindell and Barrett 1990; Meschede and Frisch 1998; Giunta *et al*. 2003). According to Platt (1993) and Thompson *et al*. (1997b), the extrusion mechanism is also driven by the angle between the plate boundary and the displacement vector. Moreover, oblique convergence has been interpreted to account for mélange formation and dispersal of high-grade blocks in the subduction channel (Cloos 1982). In the oblique convergent plate the low ratio of pure/simple shear typically implies long-lived exhumation and longer periods during which metamorphic heating occurs. The pervasive re-equilibration of the studied rocks from the NFMZ mélange during the D2 phase and the rare relict of the D1 phase fit very well with long-lived, slow exhumation as required by the oblique convergence.

The interpretation of the D3 phase is more puzzling. This phase is characterized by shortening normal to plate margins associated with very low-grade metamorphic assemblages that indicate a shallower deformation level with respect to that of the D2 phase (Figure 11). This phase can be interpreted as the final stage of the extrusion process, as detected, for instance, in the Cycladic Blueschists, Greece by Gessner *et al*. (2001) or in the Schistes Lustres from Corsica Island by Levi *et al*. (2007). The development of the D3 phase as result of a change in the geodynamic process, as for instance the transition from oblique to pure convergence or a change of the features of the underthrusted lithosphere, can be also regarded as a suitable working hypothesis to explain this deformation.

5.4. The exhumation mechanism: the D4 phase

The D4 phase, characterized by flat-lying axial-planes and horizontal fold axes represents the last pre-Eocene deformation. This deformation can be interpreted as having originated from vertical shortening and folding of preexisting non-horizontal layers, during ductile extensional tectonics (Figure 11). This is in agreement with the association of the D4 folds with the low-angle brittle shear zone showing normal fault motion with a top-to-the-NW sense of shear. This finding and the ENE-WSW trend of the D4 folds indicate the extension was at a high-angle to the plate boundary, different from that stated for the D2 phase. This type of deformation is recognized in several orogenic belts as in the Alps (Ratschbacher *et al*. 1989; Froitzheim, 1992; Wheeler and Butler 1994), in Corsica (Malavieille *et al*. 1998; Marroni and Pandolfi 2003) and also in the Caribbean area (Ellero *et al*. 2007). Many examples of fragments of oceanic lithosphere exhumed after their underplating at depth are characterized by extensional tectonics only at very shallow structural levels in the final stage of the exhumation history, as described, for instance, in the Maksyutov Complex from southern Urals, Russia by Hetzel *et al*. (1998), in the Schistes Lustres from Corsica, France (Levi *et al*. 2007), in the Tacagua unit from Cordillera de la Costa, Venezuela (Ellero *et al*. 2007) and in the Samanà peninsula from the Dominican Republic (Goncalvez *et al*. 2000).

5.5. When and how the relationships between metasedimentary rocks, eclogites and jadeitites were acquired?

The NMFZ mélange is characterized by blocks of eclogite and jadeitite set in a matrix consisting of metaserpentinites and metasedimentary rocks. Some insights about the origin of this association can be deduced by comparing the climax metamorphism of the different lithologies. Firstly, the metamorphism connected with the D1 phase identified in the metasedimentary rocks, i.e. 206–263°C and 1.00–1.25 GPa, is significantly lower than those detected in the eclogites and in the jadeitites. In these rocks the estimated P–T conditions of the metamorphic climax is 2.00–2.30 GPa and 600–650°C for the eclogites and $100 < T < 400$°C and $0.50 < P < 1.10$ GPa for the jadeitites, demonstrating a clear metamorphic decoupling between the matrix and the mélange blocks. So, the NMFZ mélange can be regarded as an assemblage of rocks showing different climax metamorphic conditions, i.e. the mélange grew by collecting lithologies deformed and metamorphosed at different depths, as observed in the Alps (e.g. Schwartz *et al*. 2001; Federico *et al*. 2007) or in the Northern Serpentinite Mélange from Cuba and Hispaniola islands (e.g. Gorczyk *et al*. 2007; Krebs *et al*. 2008).

DOI: 10.1002/gj

A model of flow mélange formation in a subduction channel (Cloos 1982; Cloos and Shreve 1988) seems to be most suitable to be applied to the NMFZ mélange (Figure 11). The mainly ductile nature of deformation in the matrix and the shale-rich sedimentary sequence involved in the subduction and accretion processes support the interpretation of a forced convection of sediments between the downgoing plate and the hanging-wall package of already accreted rocks. This circulation would produce not only the detachment and uplift of high-grade blocks but also their mixing into the ductile metasedimentary matrix. Following the model proposed by Cloos (1982) the velocity field of the flow mélange in the subduction channel is characterized by a downward flow faster than the up going flow, indicating that, through time, particles with different size, density and shape will follow different paths and will disperse differently into the flow. Moreover, oblique convergence would cause the trajectories followed by the blocks to be elliptical, enhancing their dispersion along strike. In Cloos' flow model most of the deformation in the matrix and breakup with incorporation of blocks occurs when flow reverses at depth. The high confining pressure and strain would cause plucking of blocks from the hanging wall, their rounding and dispersion. Blocks of varying metamorphic grade, from slices already accreted to the prism, could be incorporated in the flow mélange from many points at different times, and be mixed together depending on their size, shape and density. The structural evidences indicate that the coupling of different blocks occurred during the D2 phase, i.e. during the development of the S2 foliation that wraps all the blocks of the mélange. So, the D2 phase can be regarded as the deformation able to produce the mixing of different rocks. The shallower P–T conditions established in the matrix for D2 formation, seems to support incorporation and mixing of blocks during the exhumation phases, as a result of reverse flow and upward trajectory in the subduction channel (Figure 11).

6. CONCLUSIONS

The NMFZ mélange consists of blocks of eclogite and jadeitite set in a matrix composed of metaserpentinites and metasedimentary rocks. All these lithologies, that can be regarded as remnants of an oceanic lithosphere and its sedimentary cover show different climax metamorphic conditions, pointing out that the mélange grew by collecting lithologies deformed at different depths. The metasedimentary rocks include different lithologies ranging from pure quartzite to mica-rich quartzite, quartz-rich micaschist and micaschist. Paragneiss and marble are also recognized. These metasedimentary rocks display a complex deformation history, including four phases from D1 to D4. The D1 phase, that occurs only as relic, is characterized by a mineral assemblage developed under P–T conditions of 1.00–1.25 GPa and 206–263°C. These conditions point to a very cold geothermal gradient, that develops only during intraoceanic subduction. So, the D1 phase can be interpreted as related to deep underplating of a slice of oceanic lithosphere during an intraoceanic subduction. The D2 phase, characterized by isoclinal folds, schistosity and mineral/stretching lineation, developed at P–T conditions of 0.70–1.20 GPa and 279–409°C, coherent with a higher geothermal gradient, if compared with the D1 phase. According to these data, the change from D1 to D2 phase seems be corresponding to the transition from 'cold' intraoceanic subduction to the inception of 'warm' continental collision. The D2 phase and the following D3 and D4 phase, which developed at shallower structural levels, have been acquired by the NMFZ mélange during its progressive exhumation that was acquired by different mechanisms. The deformations related to the D2 phase can be regarded as having been acquired during the extrusion of the NMFZ mélange along a subduction channel during a stage of oblique subduction, as pointed out by mineral/stretching lineation characterized by a dominant strike-slip component, parallel to the plate boundary. In addition, the structural evidence indicates that the coupling and mixing of different blocks occurred during the D2 phase, as a result of reverse flow and consequent upward movement in the subduction channel. The following D3 phase developed at the final stage of this process, probably in relation to a change in the geodynamic regime. By contrast, the D4 phase can be interpreted as being related to extension at shallow structural levels. On the whole, all the structural and metamorphic data suggest that the NMFZ mélange can be regarded as fossil fragments of a subduction channel. In this framework, the exhumation-related structures in the NMFZ mélange indicate that this process, probably long-lived, developed by different mechanisms active in the subduction channel through time.

DOI: 10.1002/gj

ACKNOWLEDGEMENTS

This research was supported by M.I.U.R (Project PRIN), C.N.R (Istituto di Geoscienze e Georisorse) and funds ATENEO grant by Pisa and Florence University. The useful suggestions supplied by the reviewers L. Federico and S. Guillot improved this paper.

REFERENCES

Allemand P, Lardeaux JM. 1997. Strain partitioning and metamorphism in a deformable orogenic wedge: application to the Alpine belt. *Tectonophysics* **280**: 157–169.

Augier R, Agard P, Monie P, Jolivet L, Robin C, Booth-Rea G. 2005. Exhumation, doming and slab retreat in the Betic Cordillera (SE Spain): *in situ* $^{40}Ar/^{39}Ar$ ages and *P–T*-d-t paths for the Nevado-Filabride complex. *Journal of Metamorphic Geology* **23**: 357–381.

Avé Lallemant HG, Guth R. 1990. Role of extensional tectonics in exhumation of eclogites and blueschists in an oblique subduction setting: Northeast Venezuela. *Geology* **18**: 950–953.

Banno S, Sakai C, Higashino T. 1986. Pressure-temperature trajectory of the Sanbagawa metamorphism deduced from garnet zoning. *Lithos* **19**: 51–63.

Beccaluva L, Bellia S, Coltorti M, Dengo G, Giunta G, Mendez J, Romero J, Rotolo S, Siena F. 1995. The northwestern border of the Caribbean plate in Guatemala: new geological and petrological data on the Motagua ophiolitic belt. *Ofioliti* **20**: 1–15.

Berman RG. 1988. Internally-consistent thermodynamic data for stoichiometric minerals in the system Na2O-K2O-CaO-MgO-FeO-Fe2O3-Al2O3-SiO2-TiO2-H2O-CO2. *Journal of Petrology* **29**: 445–522.

Berman RG. 1990. Mixing properties of Ca-Mg-Fe-Mn garnets. *American Mineralogist* **75**: 328–344.

Berman RG. 1991. Thermobarometry using multiequilibrium calculations: a new technique with petrologic applications. *Canadian Mineralogist* **29**: 833–855.

Bucher K, Frey M. 2002. *Petrogenesis of metamorphic rocks*. Springer Eds., New York.

Burke K. 1988. Tectonic evolution of the Caribbean. *Annual Reviews in Earth and Planetary Sciences* **16**: 201–230.

Chemenda AI, Mattauer M, Malavieille J, Bokun AN. 1995. A mechanism for syn-collisional rock exhumation and associated normal faulting: results from physical modelling. *Earth Planetary Science Letters* **132**: 225–232.

Chemenda AI, Mattauer M, Bokun A. 1996. Continental subduction and a mechanism for exhumation of high-pressure metamorphic rocks: new modeling and field data from Oman. *Earth Planetary Science Letters* **143**: 173–185.

Chemenda AI, Burg JP, Mattauer M. 2000. Evolutionary model of the Himalaya–Tibet system: geopoem based on new modelling, geological and geophysical data. *Earth Planetary Science Letters* **174**: 397–409.

Chiari M, Dumitrica P, Marroni M, Pandolfi L, Principi G. 2007. Paleontological evidences for a Late Jurassic age of the Guatemala ophiolites. *Ofioliti* **32**: 141–150.

Clift P, Vannucchi P. 2004. Controls on tectonic accretion versus erosion in subduction zones; implications for the origin and recycling of the continental crust. *Review of Geophysics* **42**: art. N°R G2001.

Cloos M. 1982. Flow melanges: numerical modelling and geological constraints on their origin in the Franciscan subduction complex. *Geological Society of America Bulletin* **93**: 330–345.

Cloos M, Shreve RL. 1988. Subduction channel model of prism accretion, mélange formation, sediment subduction, and subducting erosion at convergent plate margins: 1. Background and description. *Pure and Applied Geophysics* **128**: 455–500.

Donnelly TW, Horne GS, Finch RC, Lopez-Ramos E. 1990. Northen central America: the Maya and Chortis blocks. In *The Caribbean Region*, Dengo G, Case JE (eds). The Geological Society of America Inc.,: Boulder, Colorado; volume **H**: 37–76.

Dengo G. 1985. Mid America: tectonic setting for the Pacific margin from Southern Mexico to North Western Colombia. In *The Ocean Basin and Margins*, Nairn AEM, Stehli FG, Uyeda S (eds). Plenum Press: New York, **7**: 15–37.

Ellero A, Malasoma A, Marroni M, Pandolfi L, Urbani F. 2007. Tectono-metamorphic history of the Tacagua ophiolitic unit (Cordillera de la Costa, Northern Venezuela): insights in the evolution of the southern margin of the Caribbean plate. *The Island Arc* **16**: 105–123.

Enami M. 1998. Pressure-temperature path of Sanbagawa prograde metamorphism deduced from grossular zoning of garnet. *Journal of Metamorphic Geology* **16**: 97–106.

Ernst WG. 1999. Metamorphism, partial preservation, and exhumation of ultrahigh-pressure belts. *The Island Arcs* **8**: 125–153.

Evans BW. 1990. Phase relations of epidote-blueschists. In: *Third International Eclogite Conference*, Okrusch M (ed). Elsevier: Amsterdam, The Netherlands, **25**: 3–23.

Federico L, Crispini L, Scambelluri M, Capponi G. 2007. Ophiolite mélange zone records exhumation in a fossil subduction channel. *Geology* **35**: 499–502.

Fisher D, Byrne T. 1987. Structural evolution of underthrusted sediments, Kodiak Islands, Alaska. *Tectonics* **6**: 775–794.

Froitzheim N. 1992. Formation of recumbent folds during synorogenic crustal extension (Austroalpine nappes, Switzerland). *Geology* **20**: 923–926.

Gerya TV, Stöckert B, Perchuck AL. 2002. Exhumation of high pressure metamorphic minerals in subduction channels: a numerical simulations. *Tectonics* **21**: 1056. DOI: 10.1029/2002TC001406

Gessner K, Ring U, Passchier CW, Gungor T. 2001. How to resist subduction: evidence for large-scale out-of-sequence thrusting during Eocene collision in western Turkey. *Journal of Geological Society of London* **158**: 769–7784.

Giunta G, Beccaluva L, Coltorti M, Cutrupia D, Dengo G, Harlow GE, Mota B, Padoa E, Rosenfeld J, Siena F. 2003. The Motagua suture zone in Guatemala. Field trip guide-book of the IGCP 433 workshop and 2nd Italian-Latin American Geological meeting 'In memory of Gabriel Dengo' January 2002. *Ofioliti* **27**: 47–72.

Giunta G, Marroni M, Padoa E, Pandolfi L. 2003. Geological constraints for the geodynamic evolution of the southern margin of the Caribbean plate. In *The Circum-Gulf of Mexico and the Caribbean*, Bartolini C, Buffler RT, Blickwede JF (eds). AAPG Memoir. American Association of Petroleum Geologists: Tulsa, OK. **79**: 104–125.

Goncalvez P, Guillot S, Nicollet C, Lardeaux JM. 2000. Thrusting and sinistral wrenching in a pre-Eocene carribean accretionary wedge (Samana pensinsula, Dominican Republic). *Geodinamica Acta* **13**: 119–132.

Gorczyk W, Guillot S, Gerya TV, Hattori K. 2007. Asthenospheric upwelling, oceanic slab retreat and exhumation of UHP mantle rocks: insights from Greater Antilles. *Geophysical Research Letters* **34**: L211309, DOI:10.1029/2007GL031059

Harlow GE. 1994. Jadeitites and related rocks from the Motagua Fault Zone, Guatemala. *Journal of Metamorphic Geology* **12**: 49–68.

Harlow GE, Sisson VB, Hans G, Avè Lallement HG, Sorensen SS, Seitz R. 2003. High-pressure, metasomatic rocks along the Motagua Fault Zone, Guatemala. *Ofioliti* **28**: 115–120.

Harlow GE, Hemming SR, Avè Lallement HG, Sisson VB, Sorensen SS. 2004. Two high-pressure-low-temperature serpentinite-matrix mélange belts, Motagua Fault Zone, Guatemala: a record of Aptian and Maastrichtian collisions. *Geology* **32**: 17–20.

Hetzel R, Ecthler HP, Seifert W, Schulte BA, Ivanov SK. 1998. Subduction- and exhumation-related fabrics in the Paleozoic high-pressure–low-temperature Maksyutov complex, Antingan area, southern Urals, Russia. *Geological Society of America Bulletin* **110**: 916–930.

Kimura G, Rodzdestvenskiy VS, Okumura K, Melinikov O, Okamura M. 1992. Mode of mixture of oceanic fragments and terrigenous trench fill in an accretionary complex: example from southern Sakhalin. *Tectonophysics* **202**: 361–374.

Krebs M, Maresh WM, Schertl HP, Baumann A, Draper G, Ildeman B, Münker C, Trapp E. 2008. The dynamics of intra-oceanic subduction zones: a direct comparison between fossil petrological evidence (Rio San Juan Complex, Dominican Republic) and numerical simulation. *Lithos* **103**: 106–133.

Levi N, Malasoma A, Marroni M, Pandolfi L, Paperini M. 2007. Tectono-metamorphic history of the ophiolitic Lento unit (northern Corsica): evidences for the complexity of accretion-exhumation processes in a fossil subduction system. *Geodinamica Acta* **20**: 99–118.

Lieberman J, Petrakakis K. 1991. TWEEQU thermobarometry: analysis of uncertainties and application to granulites from the western Alaska and Austria. *Canadian Mineralogist* **29**: 857–887.

Mahar EM, Baker JM, Powell R, Holland TJB, Howell N. 1997. The effect of Mn on mineral stability in metapelites. *Journal of Metamorphic Geology* **15**: 223–238.

Malasoma A, Marroni M. 2007. HP/LT metamorphism in the Volparone Breccia (Northern Corsica, France): evidence for involvement of the Europe/Corsica continental margin in the Alpine subduction zone. *Journal of Metamorphic Geology* **25**: 529–545.

Malavieille J, Chemenda A, Larroque C. 1998. Evolutionary model for the Alpine Corsica: mechanism for ophiolite emplacement and exhumation of high-pressure rocks. *Terranova* **10**: 317–322.

Marroni M, Pandolfi L. 2003. Deformation history of the ophiolite sequence from the Balagne Nappe, northern Corsica: insights in the tectonic evolution of Alpine Corsica. *Geological Journal* **38**: 67–83.

Meschede M, Frisch W. 1998. A plate-tectonic model for Mesozoic and Early Cenozoic evolution of the Caribbean plate. *Tectonophysics* **296**: 269–291.

Moore JC, Byrne T. 1987. Thickening of fault zones: a mechanism of mélange formation in accreting sediments. *Geology* **15**: 1040–1043.

Parra T, Vidal O, Agard P. 2002a. A thermodynamic model for Fe-Mg dioctahedral K white micas using data from phase-equilibrium experiments and natural pelitic assemblages. *Contribution to Mineralogy and Petrology* **143**: 706–732.

Parra T, Vidal O, Jolivet L. 2002b. Relation between the intensity of deformation and retrogression in blueschist metapelites of Tinos Island (Greece) evidenced by chlorite-mica local equilibria. *Lithos* **63**: 41–66.

Pavlis TL, Bruhn RL. 1983. Deep-seated flow as a mechanism for the uplift of broad forearc ridges and its role in the exposure of high P–T metamorphic terranes. *Tectonics* **2**: 473–497.

Peacock SM. 1996. Thermal and petrological structure of subduction zones. In: *Subduction: Top to Bottom*, Bebout G, Scholl DW, Kirby SH, Platt JP (eds). Geophysical Monography Series. American Geophysical Union: Washington DC. **96**: 119–133.

Peacock SM, Wang K. 1999. Seismic consequences of warm versus cool subduction metamorphism: examples from Southwest and Northeast Japan. *Science* **286**: 937–939.

Platt JP. 1986. Dynamic of orogenic wedges and the uplift of high-pressure metamorphic rocks. *Geological Society of America Bulletin* **97**: 1037–1053.

Platt JP. 1993. Mechanics of oblique convergence. *Journal of Geophysical Research* **98**: 16239–16256.

Pindell JL, Barrett SF. 1990. Geological evolution of the Caribbean region: a plate-tectonic perspective. In: *The Caribbean Region*, Dengo G, Case JE (eds). The Geological Society of America, Inc.,: Boulder Colorado. volume **H**: 339–374.

Pindell JL, Cande SC, Pitman WC III, Rowley DB, Dewey JF, Labrecque J, Haxby W. 1988. A plate-kinematic framework for models of Caribbean evolution. *Tectonophysics* **155**: 121–138.

Ramsay JG. 1967. *Folding and Fracturing of Rocks*. McGraw-Hill: New York; 568.

Ratschbacher L, Frisch W, Neubauer F, Schmid SM, Neugebauer. 1989. Extension in compressional orogenic belts: the Eastern Alps. *Geology* **17**: 404–407.

Rimmelé G, Parra T, Goffé B, Oberhänsli R, Jolivet L, Candan O. 2005. Exhumation paths of high pressure-low temperature rocks from the Lycian Nappes and the Menderes Massif (SW Turkey): a multi-equilibrium approach. *Journal of Petrology* **46**: 641–669.

Sakai C, Banno S, Toriumi M, Higashino T. 1985. Growth history of garnet in pelitic schists of the Sanbagawa metamorphic terrain in central Shikoku. *Lithos* **18**: 81–95.

Schneider J, Bosch D, Monié P, Guillot S, Garcia-Casco AG, Lardeaux JM, Torres-Roldan RL, Millan T. 2004. Origin and evolution of the Escambray massif (Central Cuba): an example of HP/LT rocks exhumed during intraoceanic subduction. *Journal of Metamorphic Geology* **22**: 227–247.

Schwartz S, Allemand P, Guillot S. 2001. Numerical model of the effect of serpentinites on the exhumation of eclogitic rocks: insights from the Monviso ophiolitic massif (Western Alps). *Tectonophysics* **42**: 193–206.
Shibakusa H, Maekawa H. 1997. Lawsonite-bearing eclogitic metabasites in the Cazadero area, northern California. *Mineralogy and Petrology* **61**: 163–180.
Silver EA, Ellis MJ, Breen NA, Shipley TH. 1985. Comments on the growth of accretionary wedges. *Geology* **13**: 6–9.
Song SG, Zhang LF, Niu Y, Wei CJ, Liou JG, Shu GM. 2007. Eclogite and carpholite-bearing metasedimentary rocks in the North Qilian suture zone, NW China: implications for Early Palaeozoic cold oceanic subduction and water transport into mantle. *Journal of Metamorphic Geology* **25**: 547–563.
Spear FS, Cheney JT. 1989. A petrogenetic grid for pelitic schists in the system SiO2–Al2O3–FeO–MgO–K2O–H2O. *Contributions to Mineralogy and Petrology* **101**: 149–164.
Symmes GH, Ferry JM. 1992. The effect of whole-rock MnO content on the stability of garnet in pelitic schists during metamorphism. *Journal of Metamorphic Geology* **10**: 221–237.
Thompson AB, Schulmann K, Jezek J. 1997a. Extrusion tectonics and elevation of lower crustal metamorphic rocks in convergent orogens. *Geology* **25**: 491–494.
Thompson AB, Schulmann K, Jezek J. 1997b. Thermal evolution and exhumation in obliquely convergent (transpressive) orogens. *Tectonophysics* **280**: 171–184.
Trotet F, Vidal O, Jolivet L. 2001a. Exhumation of Syros and Sifnos metamorphic rocks (Cyclades, Greece). New constraints on the P–T paths. *European Journal of Mineralogy* **13**: 901–920.
Trotet F, Jolivet L, Vidal O. 2001b. Tectono-metamorphic evolution of Syros and Sifnos Islands (Cyclades, Greece). *Tectonophysics* **338**: 179–206.
Tsujimori T, Liou JG, Coleman RG. 2004. Comparison of two contrasting eclogites from the Motagua Fault Zone, Guatemala: southern lawsonite eclogite versus northern zoisite eclogite. *Geological Society of America Abstracts with Programs* **36**: 136.
Tsujimori T, Liou JG, Coleman RG. 2005. Coexisting retrograde jadeite and omphacite in a jadeite-bearing lawsonite eclogite from the Motagua Fault Zone, Guatemala. *American Mineralogist* **90**: 836–842.
Tsujimori T, Sisson VB, Liou JG, Horlow GE, Sorensen SS. 2006a. Very-low-temperature record of the subduction process: a review of worldwide lawsonite eclogites. *Lithos* **92**: 609–624.
Tsujimori T, Sisson VB, Liou JG, Horlow GE, Sorensen SS. 2006b. Petrologic characterization of Guatemalan lawsonite eclogite: eclogitization of subducted oceanic crust in a cold suduction zone. *Geological Society of America, Special Paper* **403**: 147–168.
Usui T, Nakamura E, Kobayashi K, Maruyama S, Helmstaedt H. 2003. Fate of the subducted Farallon plate inferred from eclogite xenoliths in the Colorado Plateau. *Geology* **31**: 589–592.
Vidal O, Parra T. 2000. Exhumation paths of high-pressure metapelites obtained from local equilibria for chlorite-phengite assemblages. *Geological Journal* **35**: 139–161.
Vidal O, Parra T, Trotet F. 2001. A thermodynamic model for Fe-Mg aluminous chlorite using data from phase equilibrium experiments and natural pelitic assemblages in the 100–600°C, 1–25 kbar P–T range. *American Journal of Science* **301**: 557–592.
Vidal O, Parra T, Vieillard P. 2005. Experimental data on the Tschermak solid solution in Fe-chlorites: application to natural examples and possible role of oxidation. *American Mineralogist* **90**: 359–370.
Vidal O, De Andrade V, Lewin E, Munoz M, Parra T, Pascarelli S. 2006. P–T-deformation-Fe3+/Fe2+ mapping at the thin section scale and comparison with XANES mapping: application to a garnet-bearing metapelite from the Sanbagawa metamorphic belt (Japan). *Journal of Metamorphic Geology* **24**: 669–683.
Von Huene R, Scholl DW. 1991. Observations at convergent margins concerning sediment subduction, subduction erosion, and the growth of continental crust. *Reviews of Geophysics* **29**: 279–316.
Wei CJ, Powell R, Clarke GL. 2004. Calculated phase equilibria for low- and medium-pressure metapelites in the KFMASH and KMnFMASH systems. *Journal of Metamorphic Geology* **22**: 495–508.
Wheeler J, Butler RWH. 1994. Criteria for identifying structures related to true extension in orogens. *Journal of Structural Geology* **16**: 1023–1027.
Willner AP. 2005. Pressure-temperature evolution of a Late Palaeozoic paired metamorphic belt in North-Central Chile (34°–35°30'S). *Journal of Petrology* **46**: 1805–1833.
Zack T, Rivers T, Brumm R, Kronz A. 2004. Cold subduction of oceanic crust: implications from a lawsonite eclogite from the Dominican Republic. *European Journal of Mineralogy* **16**: 909–916.

DOI: 10.1002/gj